

# Turbulent Mixed Convection Heat Transfer in the presence of Rough Walls

A Numerical Study

Kyprianos Dimou

Delft University of Technology

# Turbulent Mixed Convection Heat Transfer in the presence of Rough Walls

A Numerical Study

by

Kyprianos Dimou

Student Number:

5328810

in partial fulfilment of the requirements for the degree of

Master of Science

in Mechanical Engineering  
track of

Energy, Flow & Process Technology

at the Delft University of Technology

to be defended publicly on the 31st of October 2022

Supervisor: Dr.Ir.J.W.R.Peeters

Thesis Committee: Dr.Ir.R.Pecnik

Dr.Ir.M.J.B.M.Pourquie

Faculty: Faculty of Mechanical, Maritime and Materials Engineering, TU Delft



# Abstract

Nowadays, climate change and global warming phenomena are becoming more and more serious issues. In order to sustain the enormous worldwide energy demand, society consumes a high amount of fuel, resulting into the steep increase of the level of CO<sub>2</sub> in the environment. Therefore, the massive greenhouse gases emissions in the atmosphere, generated by burning fossil at a great pace, are the main reason behind the previously mentioned phenomena.

Heat transfer augmentation methods can considerably contribute to the decrease of fuel consumption, resulting into a reduction of the greenhouse gases emissions. Therefore, this can be an effective approach to tackle the climate change and global warming phenomena. Particularly, rough surfaces are a well known heat transfer augmentation technique. Such surfaces induce turbulence and thereby the flow is well mixed. This mechanism assists convective heat transfer and as a result, heat transfer is augmented. In addition, buoyancy-influenced turbulent flows frequently occur in many engineering applications. These flows combine natural and forced convection which are due to buoyancy and the bulk flow respectively and contribute both to heat transfer. Particularly, buoyancy-aided flows can promote laminarization and therefore heat transfer deterioration.

The main focus of this study is to examine the impact of surface roughness and buoyancy effects on turbulent heat transfer. Initially, a 3D rectangular channel is considered with the streamwise, wall normal and spanwise dimensions being  $5.63 \times 2 \times 2.815$ . Subsequently, two different wall roughness geometries are constructed. Both of them have a sinusoidal shape, however the direction of travel is in the streamwise direction for the one and in the spanwise for the other. Moreover, the surface roughness is placed on the top and bottom isothermal walls of the geometry. Regarding the space and time discretization, central differences are used for the former one and second order Adams-Bashforth for the latter one. Finally, the immersed boundary method is utilized in order to incorporate the surface roughness. A series of direct numerical simulations is performed to gain an insight on how surface roughness and buoyancy forces affect the heat transfer.

The results display that both roughness schemes enhance heat transfer. Particularly, the Reynolds stresses show an increase in both rough wall cases, signifying that mixing is improved. In addition, the turbulent heat flux as well as the Nusselt numbers also exhibit a growth for both streamwise and spanwise orientation, implying that heat transfer is augmented.

Comparing the streamwise and spanwise orientations with each other, both Reynolds stresses and turbulent heat flux graphs are significantly higher in the streamwise roughness case. Moreover, the streamwise roughness is enhancing the Nusselt number approximately 1.8 times more than the spanwise roughness for the zero-buoyancy case and approximately 1.4 times more for the buoyancy-aided scenario.

Noteworthy is the fact that, the results show that the buoyancy-aided case predicts larger Reynolds stresses, turbulent heat flux and Nusselt numbers for all of the surfaces.

# Acknowledgements

I wish to express my gratitude to my academic advisor, Dr.Ir.J.W.R.Peeters for giving me the opportunity to collaborate with him. I deeply respect him as an individual and a researcher. Even though he has a busy schedule, he would always find time to guide and support me whenever I needed him.

Kyprianos Dimou  
Delft, October 2022

# Contents

Abstract	ii
Acknowledgements	iii
1 Introduction	1
1.1 Introduction . . . . .	1
1.2 Buoyancy-Influenced Turbulent Flows . . . . .	3
1.3 Heat Transfer Enhancement Techniques . . . . .	5
1.4 Passive Techniques . . . . .	6
1.5 Regular Roughness . . . . .	7
1.6 Irregular Roughness . . . . .	8
1.7 Numerical Studies . . . . .	10
1.8 Main Objective of the current Thesis . . . . .	12
2 Methodology	14
2.1 Governing Equations . . . . .	14
2.2 Direct Numerical Simulation . . . . .	16
2.3 Numerical Implementation . . . . .	17
2.3.1 Central Difference Method . . . . .	17
2.3.2 Second order Adams-Bashforth, Pressure Projection Method . . . . .	18
2.4 Immersed Boundary Method . . . . .	19
2.5 Mean statistics - Averaging Procedure . . . . .	20
2.6 Validation . . . . .	21
2.7 Simulations-Geometry . . . . .	23
2.8 Mesh . . . . .	27
2.9 Boundary Conditions . . . . .	28
3 Results-Discussion	29
3.1 Smooth VS Streamwise, $Ri=0$ . . . . .	31
3.2 Smooth VS Spanwise, $Ri=0$ . . . . .	35
3.3 Smooth VS Streamwise, $Ri=-0.8$ . . . . .	38
3.4 Smooth VS Spanwise, $Ri=-0.8$ . . . . .	42
3.5 Streamwise roughness VS Spanwise roughness . . . . .	45
3.6 Nusselt number calculation . . . . .	47
3.7 Does the buoyancy-aided flow promote laminarization? . . . . .	49
4 Conclusions, Suggestions	52
4.1 Conclusions . . . . .	52
4.2 Suggestions . . . . .	53
References	54

# List of Figures

1.1	Global CO <sub>2</sub> emissions by fuel type in billions of tonnes per year [2]. . . .	1
1.2	Two channels with heated walls. Gravity is pointing downwards, thus natural convection due to buoyancy has an upward direction. Left channel: buoyancy-assisted flow where natural convection is aligned with the bulk flow. Right channel: buoyancy-opposed flow where natural convection is opposed to the bulk flow. . . . .	3
1.3	Zhang’s set up. Four groups of heaters are placed on two opposite sides of the square channel to generate asymmetric heating conditions [65]. . .	4
1.4	Jackson’s explanation on why heat transfer deterioration occurs in the buoyancy-assisted flow. As the buoyant layer becomes thicker, the shear stress is reduced and turbulence is not maintained leading to heat transfer impairment [26]. . . . .	5
1.5	Pipes with different passive techniques for heat transfer enhancement [66].	6
1.6	Owen’s model states that horseshoe eddies wrap themselves round the individual roughness elements and scour the area, leading to a heat transfer augmentation [44]. . . . .	8
1.7	Stanton number for truncated cones (left) and hemispherical protrusions (right) for different Reynolds numbers. Clearly, there is an increase in the Stanton number for both type of elements, in respect to the smooth wall Stanton curve [25]. . . . .	9
1.8	Mean temperature with respect to distance from the wall. The mean temperature far away from the wall ( $y^+ > 10$ ) decreases with increased roughness $k^+$ [45]. . . . .	11
1.9	Recirculation zones are produced and draw heat from the bulk of the fluid to decrease the temperature gradients and improve the heat transfer [45].	12
2.1	Schematic of a 2D staggered grid. . . . .	17
2.2	A 2D example of the discrimination of the staggered grid points. Solid points are represented by black stars, bulk points by blue stars and forcing points by red stars. Note the signed distance function $\psi$ which is positive in the bulk domain and negative in the solid domain. . . . .	19
2.3	The velocity of the forcing point $P_F$ is determined by the Lagrange interpolating polynomial method. The polynomial is constructed based on three points: the two bulk points $P_1, P_2$ which are located above the forcing point and the projection of the forcing point on the solid boundary $P_B$ . . . . .	20

2.4	Graphic representation of the computational domain of Thakkar's study. On the top, a schematic of the wall-roughness of the channel is illustrated. On the bottom, the $x-z$ plane is viewed. The red dashed lines denote the top and bottom mean reference planes and the blue dash-dot line denotes the center line of the channel [57]. . . . .	21
2.5	Validation of the present code with Kim's simulation of a channel with smooth walls. As observed, there is a great agreement between Kim's results and the current code. . . . .	22
2.6	Validation of the present code with Thakkar's simulation of a channel with irregular rough walls. As observed, there is a great agreement between Thakkar's results and the current code. . . . .	23
2.7	3D view of the sinusoidal roughness with the direction of travel being in the streamwise direction, parallel to the flow. . . . .	24
2.8	Different angle of view of the sinusoidal roughness with the direction of travel being in the streamwise direction, parallel to the flow. . . . .	24
2.9	3D view of the sinusoidal roughness with the direction of travel being in the spanwise direction, normal to the flow. . . . .	25
2.10	Different angle of view of the sinusoidal roughness with the direction of travel being in the spanwise direction, normal to the flow. . . . .	25
2.11	Flow configuration and geometry by Maas and Schumann [38]. . . . .	26
2.12	Schematic of the smooth wall domain with boundary conditions. The walls are kept cool with $\theta_w = 0$ , while the bulk of fluid is heated volumetrically. Periodic boundary conditions are used for the inlet and outlet. . .	28
3.1	Schematic of the geometry for the smooth wall case. $y/h=0$ is the starting point and $y/h=1$ indicates the ending point and the middle of the channel as well. . . . .	29
3.2	Schematic of the geometry for the streamwise roughness. $y/h=-0.1$ is the starting point and $y/h=1$ indicates the ending point and the middle of the channel as well. . . . .	30
3.3	Velocity profile for the smooth wall and the streamwise roughness cases, when there is zero buoyancy. . . . .	32
3.4	Reynolds stresses profile for the smooth wall and the streamwise roughness cases, when there is zero buoyancy. . . . .	32
3.5	Turbulent heat flux profile for the smooth wall and the streamwise roughness cases, when there is zero buoyancy. . . . .	33
3.6	Temperature profile for the smooth wall and the streamwise roughness cases, when there is zero buoyancy. . . . .	33
3.7	Recirculation zones are generated near the wall for the streamwise roughness case. This phenomenon can be explained as a significant reversal of the flow (denoted by the green fluid inside the black box), as a result of the adverse pressure gradient. . . . .	34
3.8	Velocity profile for the smooth wall and the spanwise roughness cases, when there is zero buoyancy. . . . .	36
3.9	Reynolds stresses profile for the smooth wall and the spanwise roughness cases, when there is zero buoyancy. . . . .	36

3.10	Turbulent heat flux profile for the smooth wall and the spanwise roughness cases, when there is zero buoyancy. . . . .	37
3.11	Temperature profile for the smooth wall and the spanwise roughness cases, when there is zero buoyancy. . . . .	37
3.12	Velocity profile for the smooth wall and the streamwise roughness cases, when the flow is buoyancy-aided. . . . .	39
3.13	Reynolds stresses profile for the smooth wall and the streamwise roughness cases, when the flow is buoyancy-aided. . . . .	40
3.14	Turbulent heat flux profile for the smooth wall and the streamwise roughness cases, when the flow is buoyancy-aided. . . . .	40
3.15	Temperature profile for the smooth wall and the streamwise roughness cases, when the flow is buoyancy-aided. . . . .	41
3.16	Velocity profile for the smooth wall and the spanwise roughness cases, when the flow is buoyancy-aided. . . . .	43
3.17	Reynolds stresses profile for the smooth wall and the spanwise roughness cases, when the flow is buoyancy-aided. . . . .	43
3.18	Turbulent heat flux profile for the smooth wall and the spanwise roughness cases, when the flow is buoyancy-aided. . . . .	44
3.19	Temperature profile for the smooth wall and the spanwise roughness cases, when the flow is buoyancy-aided. . . . .	44
3.20	Velocity profile for the streamwise and spanwise roughness cases, when there is zero-buoyancy (left) and when the flow is buoyancy-aided (right). . . . .	45
3.21	Reynolds stresses profile for the streamwise and spanwise roughness cases, when there is zero-buoyancy (left) and when the flow is buoyancy-aided (right). . . . .	46
3.22	Turbulent heat flux profile for the streamwise and spanwise roughness cases, when there is zero-buoyancy (left) and when the flow is buoyancy-aided (right). . . . .	46
3.23	Temperature profile for the streamwise and spanwise roughness cases, when there is zero-buoyancy (left) and when the flow is buoyancy-aided (right). . . . .	46
3.24	Macrobalance constructed for the calculation of the Nusselt number. . . . .	48
3.25	Reynolds stresses for the smooth wall case when there zero-buoyancy and when the flow is buoyancy-aided. . . . .	50
3.26	Reynolds stresses for the streamwise roughness case when there zero-buoyancy and when the flow is buoyancy-aided. . . . .	50
3.27	Reynolds stresses for the spanwise case when there zero-buoyancy and when the flow is buoyancy-aided. . . . .	51
3.28	Bruch's experimental investigation of the heat transfer characteristics of a cooled vertical turbulent flow of supercritical carbon dioxide. [6] . . . . .	51

# List of Tables

1.1	Thermohydraulic performance of internal integral-fins, twisted tape inserts, corrugations, dimples and compound enhancement techniques in pipes. . . . .	7
2.1	Parameters of the two validation cases. $x, y$ and $z$ denote the streamwise, wall-normal and spanwise direction, respectively. Note that the number of grid points for Thakkar's study is larger than Kim's. The reason behind this is the need to capture all the scales of motion, since the channel has irregular roughness and therefore promotes turbulence. . . . .	22
2.2	Number of grid points in each direction. $x, y$ and $z$ denote the streamwise, wall-normal and spanwise direction, respectively. . . . .	27
3.1	Nusselt number of each simulation based on the macrobalance method. .	48

# Introduction

## 1.1. Introduction

Undoubtedly, today's working society is sustained by the massive electric energy consumption. Development in urbanization is giving electricity additional importance as the main energy source. Moreover, during the last two decades there was a steep rise in fuel consumption due to population explosion. Strongly connected with that is the increase in food production and usable water; procedures that demand high amounts of energy [39][52]. However, this enormous fuel consumption comes with a price. It is well known that society experiences climate change and global warming phenomena, having both being consequences of burning fossil fuels at a great pace and generating a high amount of carbon dioxide emissions (Figure 1.1) [2].

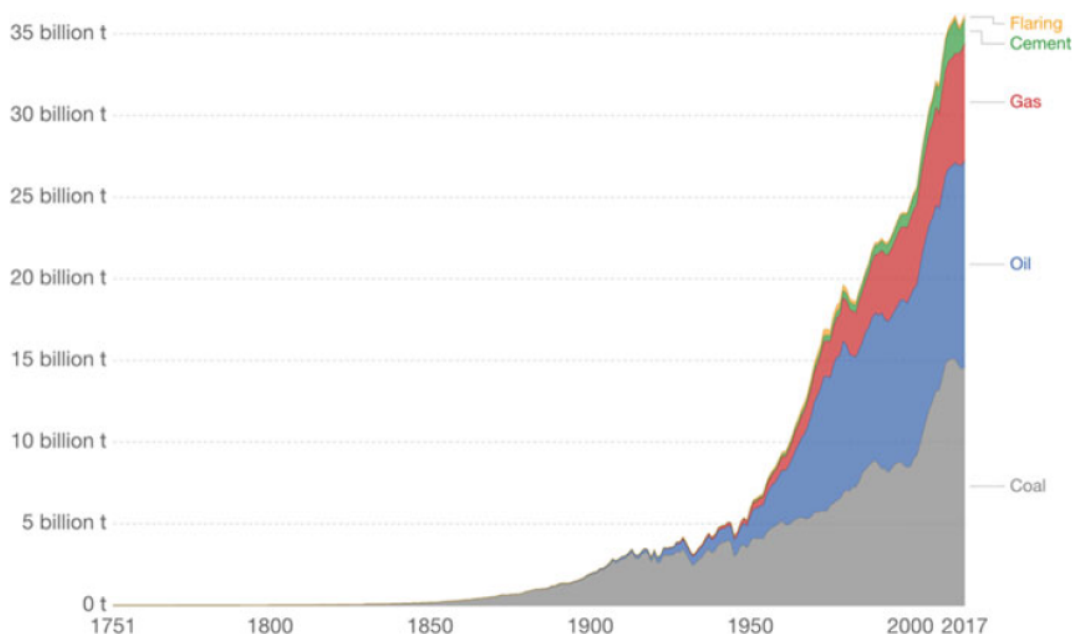


Figure 1.1: Global CO<sub>2</sub> emissions by fuel type in billions of tonnes per year [2].

Heat transfer augmentation can significantly contribute to the reduction of fuel consumption and greenhouse gas emissions [1]. During the last years, heat transfer augmentation studies gain more attention, as heat transfer is crucial to many engineering applications. It is also well known that heat transfer is extremely important to many applications regarding thermodynamic power cycles and heat pump cycles, thus maximizing the cycle requires effective heat transfer. In addition, the increased cost of energy and material generated an additional effort intended to develop more efficient heat exchange equipment. Particularly, in space applications it is necessary to miniaturize heat exchangers and this can be done through an improvement of heat transfer [18]. With the rapid evolution and increasing performance of microdevices used in electronic devices, the demand of new efficient heat transfer intensification techniques arises [3]. Regarding marine applications, fouling and scaling of heat exchangers increase the thermal resistance, resulting in searching new methods to augment heat transfer [18]. All of the above clearly state the importance of designing a compact heat exchanger, which achieves a high heat transfer rate using minimum pumping power.

A widely known heat transfer augmentation technique is rough surfaces. This technique is under the umbrella of passive methods which require no direct application of external power, in contrast to the active ones [4]. Subsequently, rough surfaces can be classified as regular or irregular. Regular rough surfaces are fundamentally surface modifications which are made intentionally, in order to induce turbulence. Having in mind that turbulence promotes mixing of the flow, while mixing of the flow assists convective heat transfer, the augmentation therefore occurs [60]. Most regular rough surfaces are discrete 3D surface indents and protrusions, based on simple geometric patterns [46][8]. However, the majority of engineering surfaces are irregular due to the level of finishing or due to erosion. The main difference from regular roughness is the fact that irregular has a completely random shape.

Heat transfer augmentation techniques are applied for forced convection, even though buoyancy-influenced turbulent flows often occur in many engineering applications. Specifically, buoyancy-influenced turbulent flows are a combination of natural and forced convection which are due to buoyancy and the bulk flow respectively and contribute both to heat transfer [27]. These flows can be separated to assisted flows where the natural convection is in the same direction as the bulk flow and to opposed flows if the two directions are opposed to each other [65]. It should be noted that the literature contains an extensive research on these types of flows within different geometries and will be discussed in detailed below.

Since, most previous fundamental research on turbulent mixed convection flow over rough surfaces is focused on regular roughness and on the momentum transfer [45], the purpose of this study is to investigate the effect of irregular roughness on turbulent mixed convection heat transfer. In the following part, research studies regarding buoyancy-influenced flows are discussed in detail. Subsequently, heat transfer enhancement techniques are mentioned with concentration on regular and irregular rough surfaces. Finally, a review of numerical studies is given, followed by details of the current thesis as well as the main objective.

## 1.2. Buoyancy-Influenced Turbulent Flows

Buoyancy-influenced turbulent flows or turbulent mixed convection flows are frequently found in the engineering industry. Particularly, these types of flows combine the forced convection and the natural convection. The forced convection originates from the bulk flow and the natural convection arises due to gravitational body forces as a consequence of a non-uniform density variation [27]. In addition, turbulent mixed convection flows are distinguished in buoyancy-assisted flows and buoyancy-opposed flows. During the buoyancy-assisted flows, natural and forced convection are aligned, while in the buoyancy-opposed flows the two are flowing in the opposite direction of each other (Figure 2).

Wang et al. [60] reported an experimental study of buoyancy-assisted and buoyancy-opposed turbulent flows within a vertical plane passage, having one wall heated and the opposite one adiabatic. Regarding the buoyancy-assisted case, increasing the influence of buoyancy resulted into a reduction in the heat transfer efficiency. Wang explained this by stating that there is a decrease in the shear stress, in the layer of buoyant fluid near the wall. Therefore, the production of turbulence is deteriorated and this negatively affects the diffusion of heat by turbulence. On the other hand, increasing the buoyancy effect in the buoyancy-opposed flow, resulted into a heat transfer enhancement, since the shear stress now increases and turbulence is induced. Similar conclusions were drawn by Kasagi et al. [32] who investigated turbulent mixed convection between two vertical parallel plates kept at different temperatures, through Direct Numerical Simulations (DNS). Zhang et al. [65] studied experimentally the buoyancy-assisted case in a vertical square channel with asymmetric heating conditions. Four heating models were created based on the combinations of four groups of heaters, placed on two opposite sides of the square channel (Figure 3). Surprisingly, even though the flow was buoyancy-assisted, Zhang observed a considerable augmentation in heat transfer, due to distortions in the flow caused by the buoyancy effect.

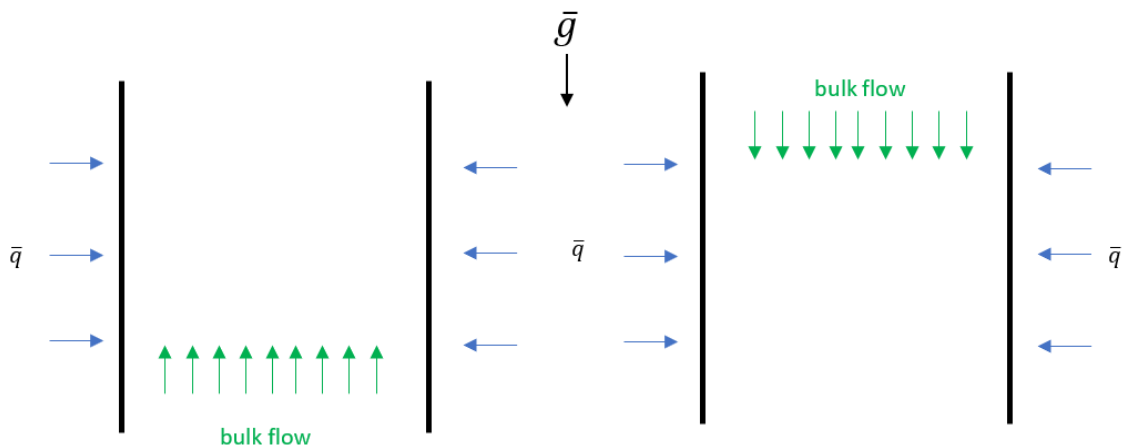


Figure 1.2: Two channels with heated walls. Gravity is pointing downwards, thus natural convection due to buoyancy has an upward direction. Left channel: buoyancy-assisted flow where natural convection is aligned with the bulk flow. Right channel: buoyancy-opposed flow where natural convection is opposed to the bulk flow.

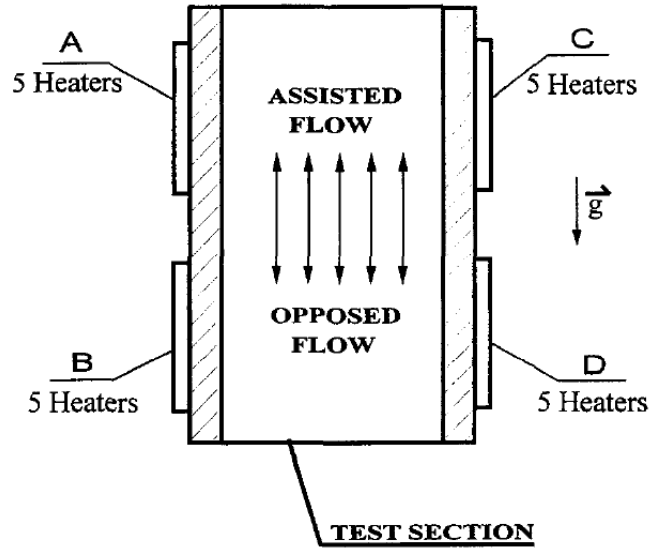


Figure 1.3: Zhang's set up. Four groups of heaters are placed on two opposite sides of the square channel to generate asymmetric heating conditions [65].

Jackson [26] presented an experimental study with uniformly heated vertical tubes, using carbon dioxide at a pressure slightly above and slightly below the critical value. The results showed that at both pressures, it was observed that there was a considerable impairment of heat transfer in the case of buoyancy-assisted flow. However, in the case of the buoyancy-opposed flow no such thing was noticed and the effectiveness of heat transfer was consistently better than with the buoyancy-assisted flow. More importantly Jackson gave a detailed explanation, similar to Wang, on why this deterioration takes place in the buoyancy-assisted flow. Jackson states that turbulence is sustained by an energy input, which arises from the shearing of the turbulent fluid. As the temperature near the wall increases, the buoyant layer becomes thicker and consequently shear stress is reduced (Figure 4). Therefore, the turbulent diffusivity  $\epsilon$  is reduced and turbulence is not maintained:

$$\epsilon = \sqrt{(\rho \times L^2 \times |\tau_t|)} \quad (1.1)$$

where  $\rho$  is the density in  $\text{kg/m}^3$ ,  $L$  is the turbulent mixing length in m and  $\tau_t$  is the turbulent shear stress in Pa. Hence, heat diffusivity also decreases leading to heat transfer deterioration.

Nieuwstadt et al. [40] explained this using the production term of the turbulent kinetic energy:

$$P_k = -\overline{u'v'} \frac{\partial \bar{u}}{\partial y} \quad (1.2)$$

where  $\overline{u'v'}$  is the time-averaged product of the velocities of the fluctuations in the directions along and normal to the wall respectively,  $\bar{u}$  is the time-averaged velocity in the direction along the wall and  $y$  is the normal distance from the wall. During the buoyancy-assisted case both fluctuation velocities as well as the gradient in the average flow (i.e. shear) are reduced in locations where a large amount of turbulence production

it is normally expected. Therefore, laminarization of the flow is promoted resulting to heat transfer impairment.

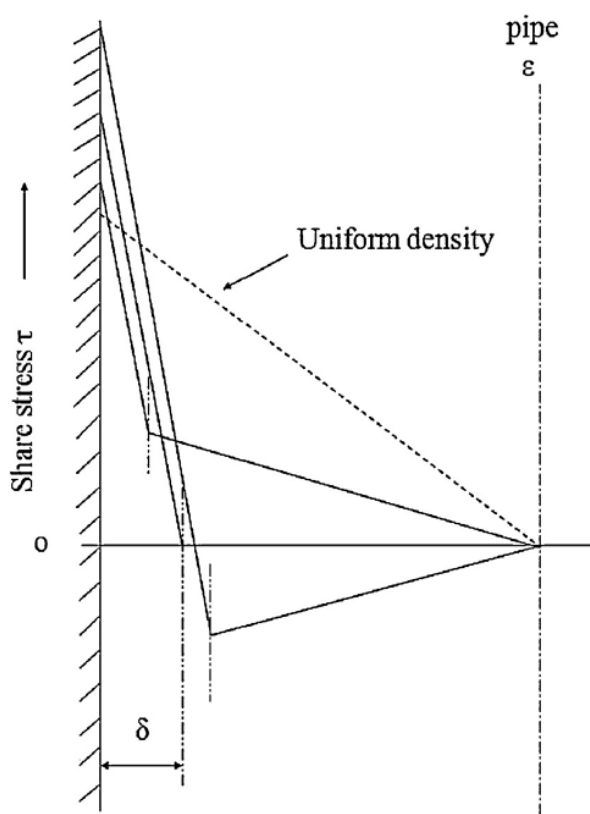


Figure 1.4: Jackson's explanation on why heat transfer deterioration occurs in the buoyancy-assisted flow. As the buoyant layer becomes thicker, the shear stress is reduced and turbulence is not maintained leading to heat transfer impairment [26].

### 1.3. Heat Transfer Enhancement Techniques

Heat transfer augmentation techniques can remarkably positively affect the engineering applications. With heat transfer enhancement the dimensions and mass of a device can be reduced considerably. In addition, there is a vital decrease in the power required to pump the heat carriers through the device, while maintaining the thermal capacity [46]. Consequently, implementing techniques which increase the heat transfer efficiency, will definitely combat the climate change and global warming phenomena which are considered as the main motives.

Various engineering industries are applying heat transfer augmentation techniques to their applications. For example, in the process industry enhanced heat transfer surfaces are used in tubes [37] and in plate heat exchangers [1]. Regarding the electronic industry, the fast evolution of microdevices causes an increased amount of heat production in this equipment. Since traditional air-cooling methods are not sufficient anymore, heat transfer enhancement methods are therefore applied [3]. Another area in which heat transfer augmentation is applied is waste heat recovery. Waste heat recovery is the process of heat integration, where the heat energy that would be dumped in the environment is

recycled back into the system [29]. Lastly, these methods are also applicable in aerospace where there is a need for miniaturization as well as in marine applications where it is common to have reduced heat transfer coefficients due to fouling [18].

Enhancement techniques can be categorized as active, passive and compound enhancement. Active techniques such as surface vibration, fluid vibration and electrostatic fields, are techniques which require external power [4]. However, these methods are not commercially viable due to cost, noise, safety, reliability and high-power consumption. The bulk of commercially feasible enhancement techniques consists of passive techniques [37]. Passive techniques opposed to the active ones, do not require external power. Nevertheless, during those methods heat transfer enhancement occurs while pressure drop increases, thus increasing the pumping power. Some of the passive techniques are rough surfaces, extended surfaces and inserts and additives like twisted tapes and wire coils (Figure 5). Finally, the third category which is compound enhancement is a combination of the above techniques. Two or more methods can be employed concurrently to generate an intensification that is usually greater than the individual methods utilized separately. An example of this category is having a rough surface with a twisted-tape swirl flow device [4]. The main objective of all these techniques is to decrease the thermal resistance of the near-wall layers by inducing turbulence and consequently increase the heat transfer coefficient.

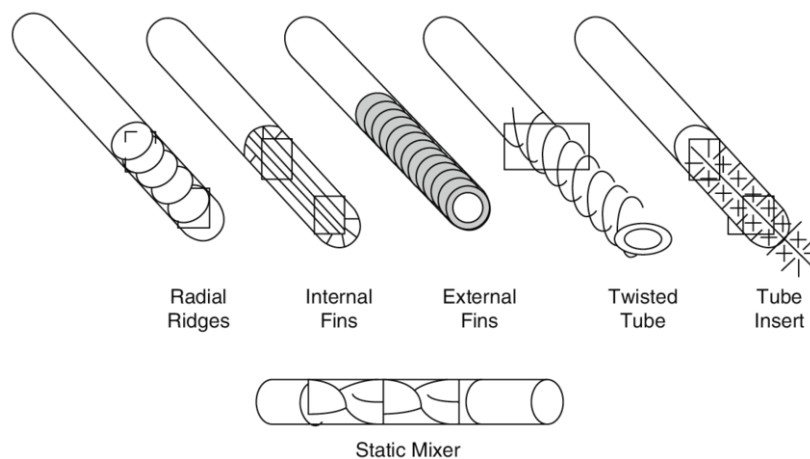


Figure 1.5: Pipes with different passive techniques for heat transfer enhancement [66].

## 1.4. Passive Techniques

More focus is given on the passive methods, since these methods are commercially viable, in contrast to the active ones. Popov et al. [46] reported a review of passive methods used for enhancing heat transfer in industrial thermal engineering devices. Popov states that for rough surfaces heat transfer can be improved by a factor of 2.5-3.5, depending on the geometrical parameters of the surface. In addition, swirling flow devices such as twisted tubes, can enhance heat transfer by a factor of 1.8-5 and coils by a factor of 1.3 to 3. Bayrak et al. [3] gave attention on surface modification techniques in a microchannel heat sink, instead of inserts and additives among passive enhancement methods. It has been concluded that, surface modification improves the convective heat transfer, however it also increases the pressure drop. Dewan et al. [18] presented a review of passive enhancement techniques, with emphasis given on twisted tapes and wire coils,

since these are economic tools. In order to compare the thermohydraulic performance of each tool, Dewan used the overall enhancement ratio which is defined as the ratio of the heat transfer enhancement ratio to the friction factor ratio:

$$\eta = \frac{Nu/Nu_0}{(f/f_0)^{1/3}} \quad (1.3)$$

where  $Nu$ ,  $f$ ,  $Nu_0$  and  $f_0$  are the Nusselt numbers and friction factors for a configuration with and without inserts respectively. In this paper it is stated that the principal thermal resistance in a turbulent flow is limited to a thin viscous sublayer near the wall and in a laminar flow is limited to a thicker region. Therefore, Dewan comes to the conclusion that wire coils are well suited for turbulent flows, since they effectively mix the flow in the viscous sublayer near the wall. Subsequently, twisted tapes are more effective in laminar flows, because they mix the bulk flow better compared to the wire coils. In addition, Wen-Tao Ji [28] reported an extensive literature survey, comparing the thermohydraulic performance of internal integral-fins, twisted tape inserts, corrugations, dimples and compound enhancement techniques in pipes. Some of the experimental results of this paper are presented in Table 1. A nice observation that can be made is the fact that for the twisted tape inserts the friction factor ratio is remarkably increased as  $Re$  increases. In contrast, the corrugated tubes show the opposite behaviour.

Researcher	$Re$	Passive Method	$f/f_0$	$Nu/Nu_0$
Prasad and Shen [47]	$35-92 \times 10^3$	Wire Coil Inserts	17.5-22.4	1.7-2.2
Chakroun and Al-Fahed [11]	$0.23-2.3 \times 10^3$	Twisted Tape	3.4-7.6	1.3-3.2
Eiamsa-ard et al. [20]	$3.7-21 \times 10^3$	Twisted Tape	5.2-8.4	2.1-2.8
Promvongse et al. [48]	$6-60 \times 10^3$	Twisted Tape	10.4-20.7	3.6-6.2
Darzi et al. [15]	$5-20 \times 10^3$	Corrugated	2.5-3.1	2.7-3.2
Kathait and Patil [33]	$7.5-50 \times 10^3$	Corrugated	2.5-2.7	1.5-2.6
Gowen and Smith [23]	$6-100 \times 10^3$	Sand Roughness	3.5-5.8	2.3-3.3
Liao et al [36]	$5-80 \times 10^3$	Extended Protrusions	3.8-4.4	2.9-3.6
Li et al [35]	$15-60 \times 10^3$	Discrete Ribs	2.8-3.5	2.0-2.1
Webb [62]	$4-24 \times 10^3$	Coned	3.6-4.6	2.6-4.5

Table 1.1: Thermohydraulic performance of internal integral-fins, twisted tape inserts, corrugations, dimples and compound enhancement techniques in pipes.

## 1.5. Regular Roughness

Regular rough surfaces are surfaces which were intentionally modified, in order to improve the heat transfer coefficient. They consist of discrete 3D surface indents and protrusions, based on simple geometric patterns such as hemispheres and truncated cones. These surface modifications not only increase the heat transfer area but most importantly induce turbulence, which helps mixing the flow and thus improves heat transfer. Owen et al. [44] proposed a simple model which describes how heat transfer is

enhanced due to surface roughness. The model consists of horseshoe eddies which wrap themselves round the individual roughness elements (Figure 6). These eddies, pull fluid down into the valley-like regions and scour the area between the adjacent protrusions. Subsequently, the fluid rises back to the roughness crests and mixes with the bulk flow. This scouring action is the mechanism behind the augmentation of heat transfer in rough surfaces.

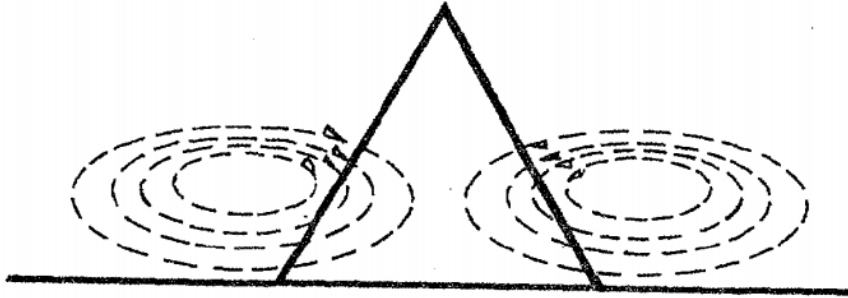


Figure 1.6: Owen's model states that horseshoe eddies wrap themselves round the individual roughness elements and scour the area, leading to a heat transfer augmentation [44].

Hosni et al. [25] used two different shapes of regular roughness: hemispherical protrusions and truncated cones. In addition, the element spacing was also varied to make the surface more or less element dense. Hosni et al. came to the conclusion that as the roughness density increases, the Stanton number also increases for both types of elements, with the hemispherical shape having slightly higher rise than the truncated cone (Figure 7). Particularly, increasing the roughness density of the truncated cones configuration could improve the Stanton number by 55% over the equivalent smooth wall case. For the hemisphere configuration, increase in the roughness density resulted into a 75% increase over the equivalent smooth wall case. To compare the data for rough surfaces with the smooth wall results, the smooth wall Stanton number expression was used:

$$St = 0.185[\log(Re)]^{-2.584} Pr^{-0.4} \quad (1.4)$$

where  $Re$  and  $Pr$  are the Reynolds and Prandtl numbers respectively.

Regarding the skin friction coefficients, surprisingly there was no increase observed for both roughness shapes and for all the roughness density variations. Scaggs et al. [51] also noted no difference in friction factor for cones and hemispheres.

## 1.6. Irregular Roughness

Most engineering rough surfaces are irregular surfaces. The reasons for this statement vary. Irregular rough surfaces can be generated due to the nature of the procedure by which they are made. In fact, grinding or boring which are considered as surface finishing processes, produce irregular surfaces even though it is expected to generate smoothness [54]. In turbomachinery applications, erosion, corrosion, pitting and fuel deposition can cause irregular roughness on the turbine blades [5]. Regarding marine

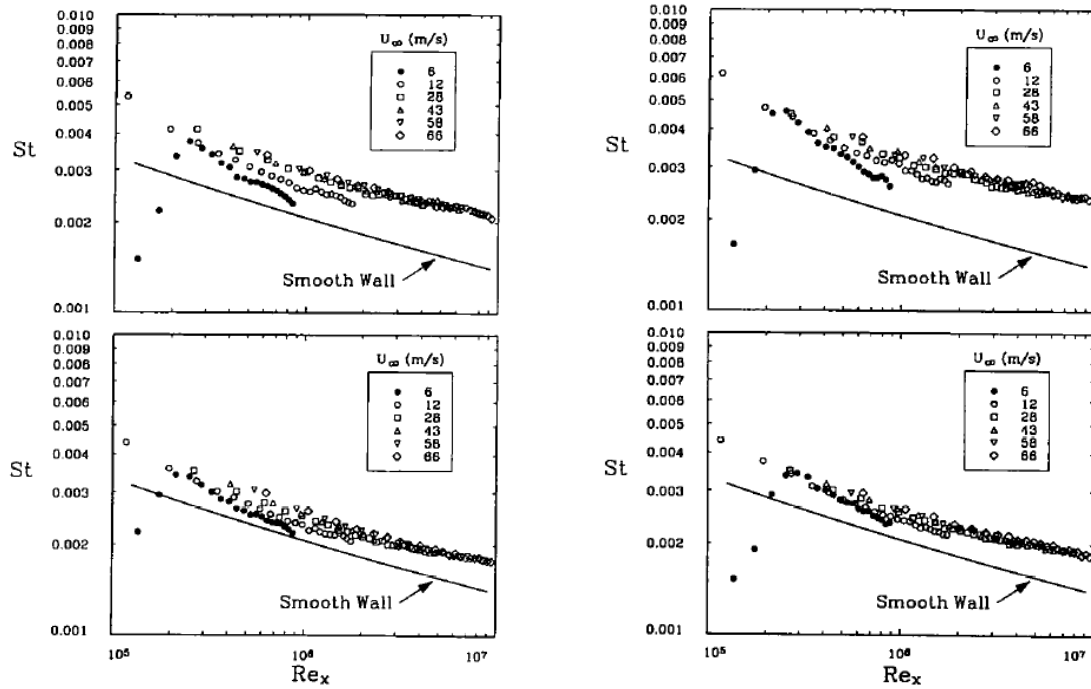


Figure 1.7: Stanton number for truncated cones (left) and hemispherical protrusions (right) for different Reynolds numbers. Clearly, there is an increase in the Stanton number for both type of elements, in respect to the smooth wall Stanton curve [25].

engineering, organic and inorganic fouling processes result in generation of roughness, which therefore is responsible for the increase in the fuel consumption [58][59]. Even on atmospheric-relevant scale, most of the urban roughness can be irregular and can influence the regional climate [12][14].

Many researches are focused on the effect of irregular roughness on pressure drop. At the beginning of the nineteenth century, Darcy carried out pressure drop experiments on pipes with different roughness. However, the groundbreaking work of correlating the impact of surface roughness on pressure drop, was conducted by Nikuradse. Nikuradse [41] constructed sand-grain roughness on the inside walls of the pipes and his work established the effect of relative roughness on the flow features. Later, important studies were reported by Colebrook and Moody, in which the Moody diagram was established as an appropriate method of evaluating the pressure drop as a function of the relative roughness [31]. In addition, Dipprey et al. [19] presented experimental results regarding the correlation between heat transfer and friction in smooth and rough tubes. For the comparison, Dipprey evaluated the heat transfer coefficient  $C_H$  and friction coefficient  $C_F$  of distilled water flowing upwards through electrically heated tubes. The experiments were conducted with surfaces having a closed-packed sand grain-type roughness. This choice was taken because the sand grain roughness simulates natural roughness due to the random shape of the elements, thus the results would be considered as an expansion of Nikuradse's work. Dipprey's results indicated that with the type of roughness used, the  $2C_H/C_F$  values can only be reduced by roughening if  $Pr < 3$ . However, if  $Pr > 3$  there is always a possibility to choose a finite roughness to acquire  $2C_H/C_F$  values higher than those for the smooth tube.

## 1.7. Numerical Studies

Computational fluid dynamics (CFD) is a powerful numerical tool which is utilized to obtain insight into fluid motion. It combines mathematical physics, numerical solutions for the Navier-Stokes equations and state-of-the-art visualization techniques, in order to accurately represent the flow [42]. Since turbulent flows are prevalent in nature and in most engineering applications, the majority of simulations require a turbulence model. Turbulent flows are characterized by a large range of vortical structures at different scales. The largest scales contain most of the kinetic energy and break into smaller ones. As this breakdown takes place, energy is transferred from the large to the small scales, until the effect of viscosity can convert the kinetic energy into thermal energy [40]. Therefore, the following numerical methods aim to solve the Navier-Stokes equations, either the full set or a reduced set of equations including modeling part of certain scales.

Direct Numerical Simulation (DNS) is the most accurate but computationally expensive numerical method for flow representation. This approach resolves both the macrostructure and microstructure without relying on any modeling of the turbulent flow. However, the computational effort for a DNS, increases almost with the cube of the Reynolds number.

$$\text{computational effort} = O(Re^{11/4}) \quad (1.5)$$

Due to this computational expensiveness, DNS has been mainly limited to low to moderate Reynolds numbers and simplified flow geometries like channels and pipes. That is also the reason why this approach is not preferred in the industry and is almost exclusively used in research institutions.

Large Eddy Simulation (LES) is another numerical technique, which is less accurate and less expensive compared to DNS. In LES, the smallest scales are filtered out while the largest scales which contain most of the energy are resolved directly [10]. This method was developed for situations in which there is an interest only in certain quantities, such as lift and drag force on an object; quantities where only the large scales should be considered as these scales carry most of the momentum.

Reynolds Averaged Navier-Stokes (RANS) is the least accurate and computationally expensive method compared to the other two. With RANS, a simpler set of the Navier-Stokes equations is solved, which is based on a time-averaged operation and on the Reynolds decomposition. However, this approach contains some additional terms called Reynolds Stresses that need to be modelled. RANS modelling is the most common and widespread approach in industrial applications as it can give large scale information about the system like the average drag or lift relatively fast [50][10].

In the literature all the above-mentioned numerical approaches are utilized in geometries with rough surfaces. Tamura et al. [56] investigated turbulent-boundary layer flows over a hill-shaped model, at moderately high Reynolds numbers using LES. Henn et al. [24] carried out LES for separated turbulent flow over wavy smooth surfaces in a channel. Gong et al. [22] studied aerodynamically rough turbulent boundary-layer flows over a sinusoidal surface, through LES. Stoesser [53] simulated turbulent channel flows over rough beds, employing again LES. Wang et al. [61] computed the skin friction and heat transfer coefficients on real rough surfaces utilizing a RANS approach. In addition, Xie et al. [63] investigated turbulent flows over wall-mounted obstacles using both LES and RANS. Comparing the two methods, Xie emphasizes that RANS provided inade-

quate and less satisfactory results compared to LES. Jin et al. [30] validated RANS models of turbulent flows in rough wall channels, based on DNS results. The critical parameters that were varied for the validation process were the Reynolds number and the non-dimensional size of the roughness elements  $k/H$  where  $k$  is the width of the element size and  $H$  is half the distance between the two walls. Orlandi et al. [43] investigated heat transfer in the presence of regular rough walls, using explicitly DNS. A research similar to the current thesis topic, was conducted by Peeters et al. [45] who investigated turbulent heat transfer in channels with irregular roughness through DNS. In this paper, a bulk heated fluid flows through a constant wall temperature channel, which consists of a grit-blasted surface. The results show that the mean temperature far away from the wall ( $y^+ > 10$ ) decreases with increased roughness  $k^+$  (Figure 8). The main reason behind this is the recirculation zones generated, which draw heat from the bulk of the fluid (Figure 9). This also agrees well with the theory as roughness induces turbulence which helps mixing the flow and increases heat transfer. In addition, this temperature downward shift can be described by the temperature wall roughness function:

$$\Delta\Theta^+ = \frac{Pr_t}{\kappa} \ln(k_s^+) + \beta'(Pr) - \frac{5}{4}(k_s^+)^{0.2} Pr^{0.44} \quad (1.6)$$

where  $Pr_t$  is the turbulent Prandtl number,  $\kappa$  is the von Karman constant,  $\beta'(Pr) = (3.85Pr^{1/3} - 1.3)^2 + (Pr_t/\kappa)\ln(Pr) - 7.4$  and  $k_s^+$  is the sand grain equivalent roughness height. In addition, Peeters also inspected the momentum wall roughness function  $\Delta U^+$ . Comparing the two wall roughness functions it was concluded that there is a difference between the two values, due to the recirculation zones. Consequently, the Reynolds analogy fails.

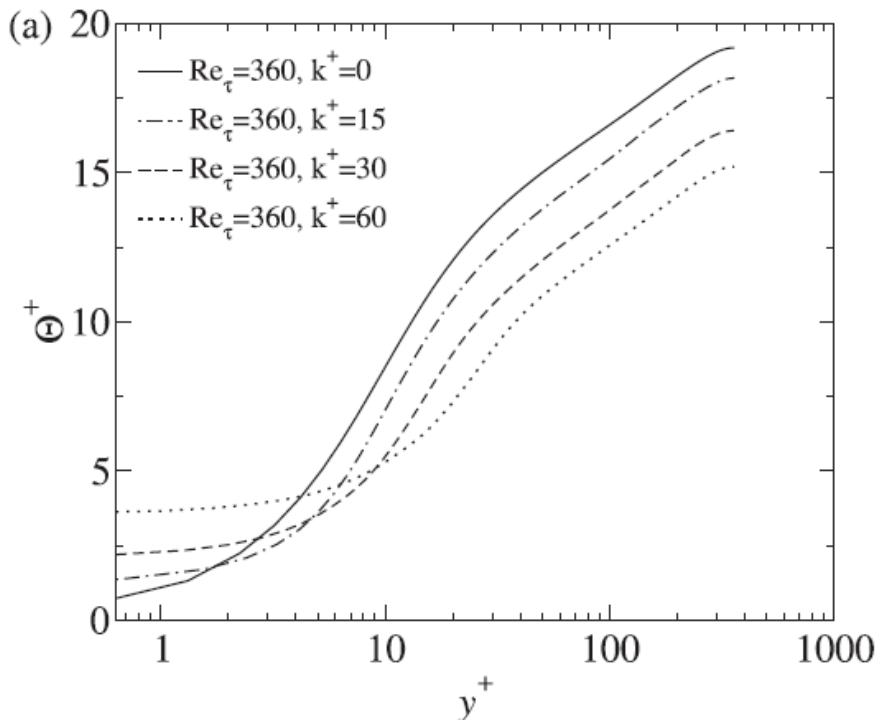


Figure 1.8: Mean temperature with respect to distance from the wall. The mean temperature far away from the wall ( $y^+ > 10$ ) decreases with increased roughness  $k^+$  [45].

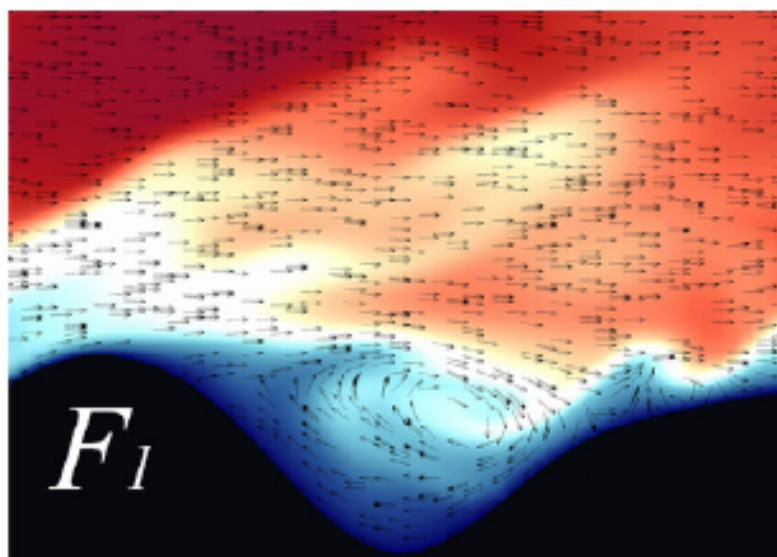


Figure 1.9: Recirculation zones are produced and draw heat from the bulk of the fluid to decrease the temperature gradients and improve the heat transfer [45].

## 1.8. Main Objective of the current Thesis

Although the impact of wall roughness on momentum transfer is being thoroughly examined, less emphasis has been given to the effect of wall roughness on turbulent heat transfer. In addition, both regular and irregular rough surfaces have been studied over the years for various reasons. For example, studying irregular rough surfaces can provide an insight on how the flow is modified when the inside of a pipe suffers from corrosion or when the level of finishing is not high. On the other hand, studying regular rough surfaces can give an indication on how the flow is altered when a certain pattern is added inside the pipe to enhance heat transfer. Moreover, buoyancy is also a parameter which should be taken into consideration, as it is found in many engineering applications and can significantly influence the results depending on its direction.

Taking all of the above into consideration, the current thesis is focused on the following objectives:

- Investigation of the impact of two different types of regular roughness on heat transfer, in turbulent mixed convection flows. Both of them have a sinusoidal shape, however the direction of travel is in the streamwise direction for the one and in the spanwise for the other. Parameters like the mean velocity, the mean temperature, the mean Reynolds stresses and the mean turbulent heat flux are examined.
- Investigation of the impact of buoyancy on heat transfer for the same types of regular roughness, in turbulent mixed convection flows. For each type of roughness, the Richardson number will be modified to have a buoyancy-aided flow. Parameters like the mean velocity, the mean temperature, the mean Reynolds stresses and the mean turbulent heat flux are examined.
- Comparison between the two different types of regular roughness regarding heat transfer.

---

In particular, for the first two objectives a series of direct numerical simulations will be executed to represent a flow past the two different regular rough surfaces, which are constructed based on a sinusoidal wave. To account for the roughness, the immersed boundary method will be used. For the last objective, the two types of roughness will be compared with each other to decide which one has the highest heat transfer augmentation.

# 2

## Methodology

### 2.1. Governing Equations

The behavior of a Newtonian fluid flow is governed by the Navier-Stokes equations. The Navier-Stokes equations describe the conservation of mass, momentum and energy. For an incompressible flow, the Navier-Stokes equations read:

$$\frac{\partial u_i}{\partial x_i} = 0 \quad (2.1)$$

$$\rho \frac{\partial u_i}{\partial t} + \rho \frac{\partial u_j u_i}{\partial x_j} = -\frac{\partial P}{\partial x_i} + \mu \frac{\partial^2 u_i}{\partial x_j \partial x_j} + \rho g_i \quad (2.2)$$

$$\frac{\partial T}{\partial t} + u_i \frac{\partial T}{\partial x_i} = \alpha \frac{\partial^2 T}{\partial x_i \partial x_i} \quad (2.3)$$

where  $i, j = 1, 2, 3$ ;  $x$  is the Cartesian position vector in m, also denoted as  $x, y, z$ ;  $u$  represents the velocity vector in m/s, also denoted as  $u, v, w$ . The gravitational acceleration  $g$  in  $\text{m/s}^2$  acts along the  $x$ -direction. In addition,  $t$  represents the time in s,  $P$  the pressure in Pa and  $T$  the temperature in K. Regarding the properties of the fluid,  $\rho$  depicts the density in  $\text{kg/m}^3$ ,  $\mu$  the dynamic viscosity in Pa·s and  $\alpha$  the thermal diffusivity in  $\text{m}^2/\text{s}$ . In summary, equations (2.1), (2.2) and (2.3) represent the conservation of mass, momentum and energy, respectively.

One way to implement buoyancy effects into the Navier-Stokes equations is to use the Boussinesq approximation. The Boussinesq approximation considers density variations only in the body force term and relates the density difference to the coefficient of thermal expansion and temperature difference. In addition, it can be applied when the density variations are small. However, the equation which describes the conservation of momentum needs to be modified before applying the Boussinesq approximation.

It is common to introduce a reference density  $\rho_r$ , which is possibly the density at some far-field free stream [17]. Then  $\rho = \rho_r + \rho - \rho_r$  and the momentum equation can be written as:

$$\rho \frac{\partial u_i}{\partial t} + \rho \frac{\partial u_j u_i}{\partial x_j} = -\frac{\partial P}{\partial x_i} + \mu \frac{\partial^2 u_i}{\partial x_j \partial x_j} + \rho_r g_i + (\rho - \rho_r) g_i \quad (2.4)$$

It should be reminded that this modification only occurs in the body force term, since the Boussinesq approximation states that the density variation is only important there. Therefore, since the density difference can be neglected in the rest of the equation, one can accept that the density in the left-hand side of the equation is equal to the reference density. Finally, assuming that the reference density is constant, equation (2.4) can be written as:

$$\rho \frac{\partial u_i}{\partial t} + \rho \frac{\partial u_j u_i}{\partial x_j} = - \frac{\partial(P - \rho_r g_i x_i)}{\partial x_i} + \mu \frac{\partial^2 u_i}{\partial x_j \partial x_j} + (\rho - \rho_r) g_i \quad (2.5)$$

In Equation (2.5), the term  $P - \rho_r g_i x_i$  portrays a reduced pressure  $\tilde{P}$ , by which the flow is driven. The benefit of this implementation is to decrease magnitudes used in the computation of momentum sources, both in the pressure gradient and in the body force term. Therefore, round-off errors are diminished [17].

The Boussinesq approximation states that the density differences can be overlooked in all but the body force term and depend exclusively on temperature differences. Consequently,

$$\Delta \rho = -\beta \rho_r \Delta T \quad (2.6)$$

or

$$\rho - \rho_r = -\beta \rho_r (T - T_r) \quad (2.7)$$

Subsequently, the thermal expansion coefficient  $\beta$  is defined as:

$$\beta = -\frac{1}{\rho_r} \frac{\partial \rho}{\partial T} \quad (2.8)$$

Substituting equation (2.8) in equation (2.5) and making use of the reduced pressure  $\tilde{P} = P - \rho_r g_i x_i$ , yields:

$$\frac{\partial u_i}{\partial t} + \rho \frac{\partial u_j u_i}{\partial x_j} = - \frac{1}{\rho_r} \frac{\partial \tilde{P}}{\partial x_i} + \nu \frac{\partial^2 u_i}{\partial x_j \partial x_j} - \beta (T - T_r) g_i \quad (2.9)$$

where  $\nu$  is the kinematic viscosity in  $\text{m}^2/\text{s}$ . It should be noted that the minus sign in front of the body force term is chosen such that equation (2.9) represents a buoyancy-opposed flow, that is a flow in which natural convection is opposed to the bulk flow.

Now that the Boussinesq approximation is applied, equations (2.1), (2.3), (2.9) are non-dimensionalised. The problem is then governed by the following dimensionless Navier-Stokes equations:

$$\frac{\partial u_i^*}{\partial x_i^*} = 0 \quad (2.10)$$

$$\rho \frac{\partial u_i^*}{\partial t^*} + \rho \frac{\partial u_j^* u_i^*}{\partial x_j^*} = - \frac{\partial \tilde{P}^*}{\partial x_i^*} + \frac{1}{Re} \frac{\partial^2 u_i^*}{\partial x_j^* \partial x_j^*} - Ri \theta^* \delta_{i3} \quad (2.11)$$

$$\frac{\partial \theta^*}{\partial t^*} + u_i^* \frac{\partial \theta^*}{\partial x_i^*} = \frac{1}{Pe} \frac{\partial^2 \theta^*}{\partial x_i^* \partial x_i^*} + \Phi \quad (2.12)$$

where  $i, j = 1, 2, 3$ ;  $x^*$  is the non-dimensional Cartesian position vector, also denoted as  $x^*, y^*, z^*$ ;  $u^*$  represents the non-dimensional velocity vector, also denoted as  $u^*, v^*, w^*$ . Moreover,  $t^*$  represents the non-dimensional time,  $\tilde{P}^*$  the reduced pressure and  $\theta^*$  the non-dimensional temperature. The scales applied to non-dimensionalise these variables are the height of the channel  $H_0 = 2h$  as the length scale, the bulk velocity  $u_0 = u_b$  as the velocity scale,  $t_0 = H_0/u_0$  as the time scale and  $P_0 = \rho_r \cdot u_b^2$  as the pressure scale. The bulk velocity is specified as:

$$u_b = \frac{\int_0^{2h} u \, dy}{\int_0^{2h} dy} \quad (2.13)$$

Temperature is formed non-dimensional as  $\theta^* = (T - T_w)/(T_b - T_w)$  where  $T_w$  is the wall temperature of the channel and  $T_b$  is the bulk temperature and is defined as:

$$T_b = \frac{\int_0^{2h} \rho u C_p T \, dy}{\int_0^{2h} \rho u C_p \, dy} \quad (2.14)$$

In addition,  $\Phi$  represents a dimensionless heat generation term, which volumetrically heats the bulk of the flow.

Using these scales, the characteristic dimensionless groups rising are the Reynolds number, Richardson number and the Peclet number:

$$Re = \frac{\text{inertial forces}}{\text{viscous forces}} = \frac{u_0 \cdot H_0}{\nu} \quad (2.15)$$

$$Ri = \frac{\text{natural convection}}{\text{forced convection}} = \frac{g \cdot \beta \cdot (T_b - T_w) \cdot H_0}{u_0^2} \quad (2.16)$$

$$Pe = \frac{\text{heat transfer by convection}}{\text{heat transfer by conduction}} = \frac{u_0 \cdot H_0}{\alpha} \quad (2.17)$$

## 2.2. Direct Numerical Simulation

The three most common numerical methods, which aim to solve the Navier-Stokes equations are the Reynolds Averaged Navier-Stokes (RANS), the Large Eddy Simulation (LES) and the Direct Numerical Simulation (DNS). As already mentioned, turbulent flows are defined by a large range of scales of motion. Particularly, the energetic large eddies break up into smaller eddies until the microstructure has been reached. Then the kinetic energy is dissipated into heat through viscous friction. Some of these numerical methods solve the full set of the equations while the others solve a reduced set and model a part of certain scales, depending on their accuracy.

Starting with RANS, it has the lowest accuracy and computational cost compared to the other two. It is based on decomposing a quantity on its time-averaged and fluctuating quantities, known as the Reynolds decomposition. Moreover, RANS method provides a time-averaged solution to the Navier-Stokes equations. Consequently, RANS is utilized to gain insight on large scale information about the system like the average drag or lift.

Subsequently, the LES method is more accurate and more computationally expensive compared to RANS. In LES the largest scales are resolved directly, while the smallest scales which contain the least energy are modelled. Similar to the RANS technique, LES

is mostly used in situations where only the large scales are considered, like the lift and drag force on a system.

Finally, DNS is the most accurate and the most computationally expensive numerical method out of the three. During the DNS method both macrostructure and microstructure are resolved without any modeling. Opposed to the other two methods, DNS is used almost exclusively for research purposes due to its relatively high computational cost.

For the purpose of this thesis, the Direct Numerical Simulation method is chosen to solve the Navier-Stokes equations and represent the flow. The reason behind this choice is the high accuracy of this method and the capability to resolve even the small scales of motion that will be generated close to the rough walls.

## 2.3. Numerical Implementation

The incompressible Navier-Stokes equations for a fluid with uniform density  $\rho$  and kinematic viscosity  $\nu$  are solved to represent the flow. For the solution, central differences are employed to discretize the spatial derivatives. The second order Adams-Bashforth scheme combined with the Pressure Projection Method are used for the time integration. The finite difference code acts on a staggered grid (Figure 2.1), in order to prevent the decoupling of pressure and velocity fields and therefore avoid the checkboard problem [21].

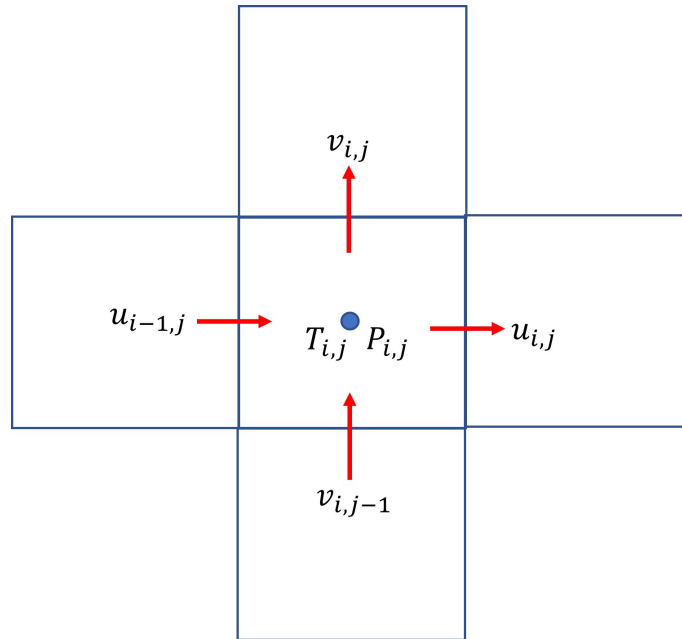


Figure 2.1: Schematic of a 2D staggered grid.

### 2.3.1. Central Difference Method

The space discretization is achieved by the Central Difference Method. Central Difference is selected instead of Forward or Backward Difference since the truncation error of the Central Difference scheme is order of  $O(h^2)$  where  $h$  is the step size, opposed to the  $O(h)$  of the other methods. Consequently, the approximation of the spatial derivatives

by the Central scheme is considerably more accurate compared to the other two.

### 2.3.2. Second order Adams-Bashforth, Pressure Projection Method

The governing equations are integrated in time explicitly with a second order Adams-Bashforth method. In addition, since there is no equation for the temporal evolution of the pressure, a coupling is formed between the pressure and velocity fields [49]. Therefore, the Pressure Projection Method is introduced to decouple the equations and split the solution into distinct steps for the velocity and pressure. The combination of the two methods will be demonstrated on the general form of the Navier-Stokes momentum equations.

The incompressible Navier-Stokes momentum equation may be written as:

$$\frac{\partial \mathbf{u}}{\partial t} + (\mathbf{u} \cdot \nabla) \mathbf{u} = -\frac{1}{\rho} \nabla P + \nu \nabla^2 \mathbf{u} \quad (2.18)$$

where  $\mathbf{u}$  is the velocity vector,  $\rho$  is the density,  $P$  is the pressure,  $\nu$  is the kinematic viscosity and  $t$  is the time. The first step of the Pressure Projection Method is the computation of an intermediate velocity  $\mathbf{u}'$  by ignoring the pressure gradient and focusing only on the convection and diffusion terms. Moreover, for the calculation of the intermediate velocity, the second order Adams-Bashforth method is utilized. The intermediate velocity  $\mathbf{u}'$  is given by:

$$\frac{\mathbf{u}' - \mathbf{u}^n}{\Delta t} = \frac{3}{2} [-(\mathbf{u}^n \cdot \nabla) \mathbf{u}^n + \nu \nabla^2 \mathbf{u}^n] - \frac{1}{2} [\mathbf{u}^{n-1} \cdot \nabla) \mathbf{u}^{n-1} + \nu \nabla^2 \mathbf{u}^{n-1}] \quad (2.19)$$

where the index  $n$  represents the current discrete time and  $\Delta t$  is the time step. Subsequently, the Pressure Poisson equation is formed and solved to obtain the pressure gradient which will be used to calculate the velocity of the next discrete time  $n + 1$ . To form the Pressure Poisson equation, the momentum equation is discretized in time, considering only the pressure term:

$$\frac{\mathbf{u}^{n+1} - \mathbf{u}'}{\Delta t} = -\frac{1}{\rho} \nabla P^{n+1} \quad (2.20)$$

Then the divergence of Equation (2.20) is taken:

$$\frac{\nabla \cdot \mathbf{u}^{n+1} - \nabla \cdot \mathbf{u}'}{\Delta t} = -\frac{1}{\rho} \nabla^2 P^{n+1} \quad (2.21)$$

Having in mind that the continuity equation  $\nabla \cdot \mathbf{u} = 0$  applies for the next discrete time, Equation (2.21) reduces to the Pressure Poisson equation:

$$\frac{-\nabla \cdot \mathbf{u}'}{\Delta t} = -\frac{1}{\rho} \nabla^2 P^{n+1} \quad (2.22)$$

Once the pressure gradient is calculated, the velocity of the next discrete time  $\mathbf{u}^{n+1}$  is given by rearranging Equation (2.20):

$$\mathbf{u}^{n+1} = \mathbf{u}' - \frac{\Delta t}{\rho} \nabla P^{n+1} \quad (2.23)$$

## 2.4. Immersed Boundary Method

To take into account the surface roughness, the immersed boundary method is applied. This method was previously used in simulations where the surface had an irregular type of roughness and again the effect on heat transfer was examined [64]. The main principle of this method is the discrimination of the staggered grid points into 3 categories (Figure 2.3):

- the solid points (black stars), which exist in the solid domain
- the bulk points (blue stars), which exist in the fluid domain and have no direct neighbor in the solid domain
- the forcing points (red stars), which exist in the fluid domain and have at least one direct neighbor in the solid domain

The classification occurs based on the signed distance function  $\psi(x, y, z)$  which is positive in the fluid domain, negative in the solid domain and zero on the boundary. The time-integration scheme for the bulk points stays the same as before. Regarding the solid points, since they represent the stationary rough wall, their velocity is set to zero. Finally, the velocity of the forcing points is defined by the Lagrange interpolating polynomial method. This method constructs a polynomial based on the existed velocity values and thereafter the velocity of the forcing points is estimated based on the polynomial. The interpolation occurs between the two bulk points in the fluid domain  $P_1, P_2$  which are located above the forcing point and the projection of the forcing point on the solid boundary  $P_B$  where the signed distance function  $\psi$  is equal to zero (Figure 2.4). Lastly, the velocity at  $P_B$  is set to zero since it is equal to the wall velocity.

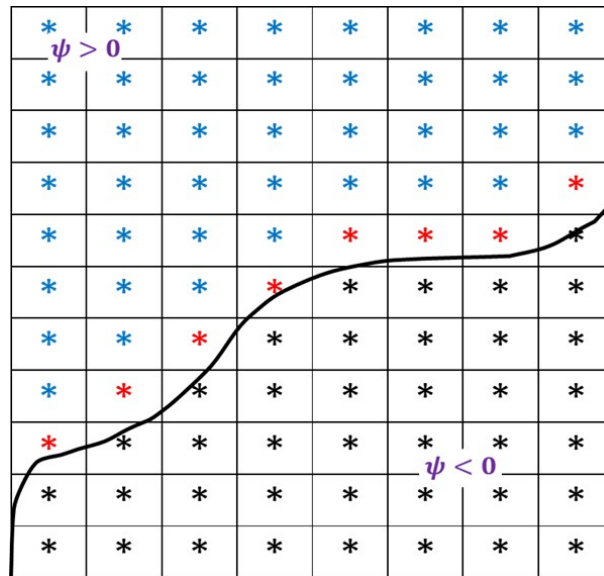


Figure 2.2: A 2D example of the discrimination of the staggered grid points. Solid points are represented by black stars, bulk points by blue stars and forcing points by red stars. Note the signed distance function  $\psi$  which is positive in the bulk domain and negative in the solid domain.

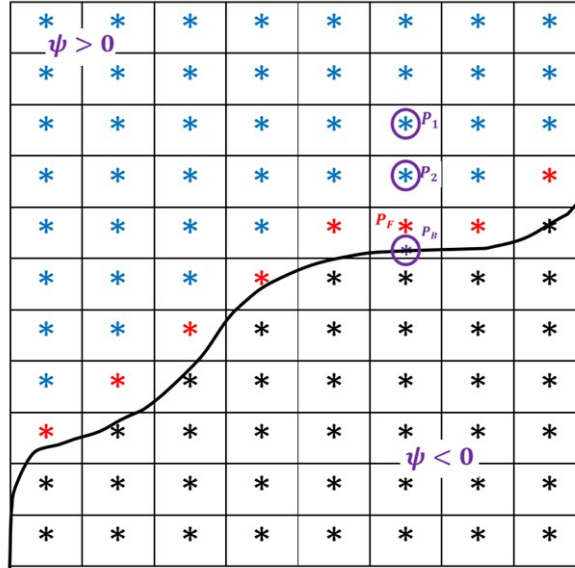


Figure 2.3: The velocity of the forcing point  $P_F$  is determined by the Lagrange interpolating polynomial method. The polynomial is constructed based on three points: the two bulk points  $P_1, P_2$  which are located above the forcing point and the projection of the forcing point on the solid boundary  $P_B$ .

## 2.5. Mean statistics - Averaging Procedure

The following averaging method is used, in order to gather the mean velocity and mean temperature statistics. The mean temperature is acquired by plane averaging the time-averaged temperature  $\bar{\theta}$  over the fluid domain:

$$\Theta = \langle \bar{\theta} \rangle = \frac{1}{A} \int_A \beta \bar{\theta} dA \quad (2.24)$$

where  $\bar{\theta}$  represents the time-averaged temperature and  $A$  denotes a plane parallel to the wall. In addition,  $\beta$  is a function which indicates whether the time-averaged quantity is located inside or outside the fluid domain. Therefore,  $\beta$  is equivalent to unity within the fluid domain and zero outside the fluid domain. Likewise,  $U$  is calculated by plane averaging the time averaged streamwise velocity  $\bar{u}$ .

The calculations of the instantaneous fluctuations of the temperature, streamwise and wall-normal velocities are given respectively by:

$$\theta' = \theta - \bar{\theta} \quad (2.25)$$

$$u' = u - \bar{u} \quad (2.26)$$

$$v' = v - \bar{v} \quad (2.27)$$

Finally, the Reynolds stresses  $\overline{u'v'}$  and turbulent heat flux  $\overline{u'\theta'}$  can be computed through the temperature and velocity fluctuations, as mentioned above.

## 2.6. Validation

The above-mentioned numerical methods were validated with two different cases. A simulation of a channel with a smooth wall, reported by Kim et al. [34] and a simulation of a channel with irregular wall roughness, reported by Thakkar et al. [57]. The surface that is considered in Thakkar's study is a filtered surface of a grit-blasted surface (Figure 2.5) and it has demonstrated to act as a surrogate for Nikuradse-type roughness.

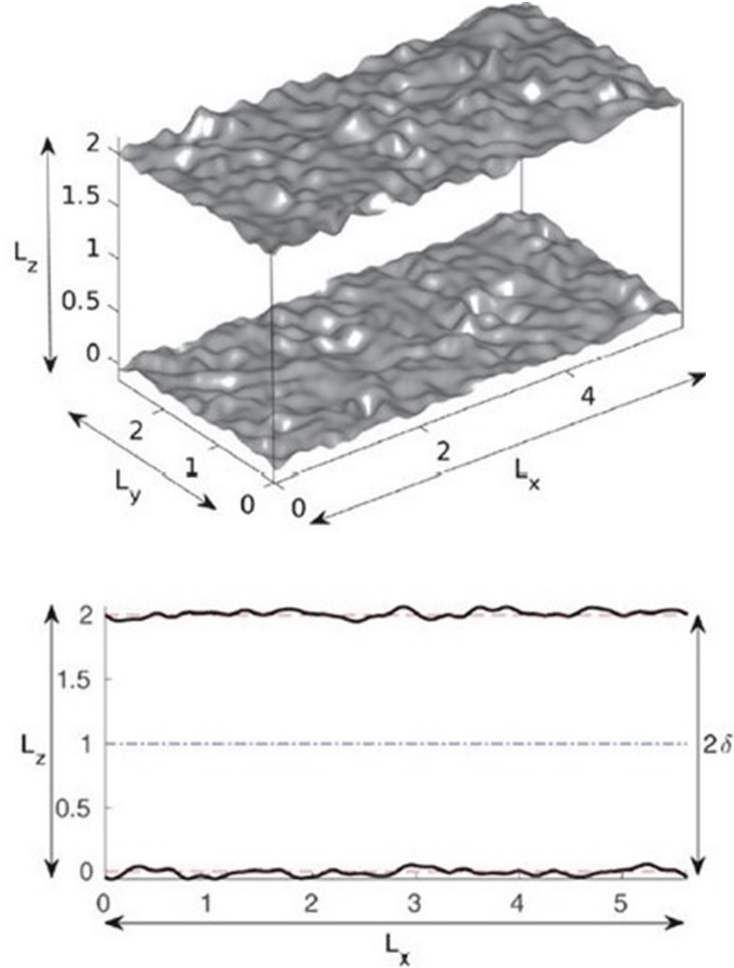


Figure 2.4: Graphic representation of the computational domain of Thakkar's study. On the top, a schematic of the wall-roughness of the channel is illustrated. On the bottom, the  $x - z$  plane is viewed. The red dashed lines denote the top and bottom mean reference planes and the blue dash-dot line denotes the center line of the channel [57].

Both studies use the friction Reynolds number instead of the bulk Reynolds number. The friction Reynolds number is given by:

$$Re_\tau = \frac{u_\tau \cdot \delta}{\nu} \quad (2.28)$$

where  $u_\tau$  is the friction velocity,  $\delta$  is half the height of the channel and  $\nu$  is the kinematic viscosity. During the validation process the friction Reynolds number was set to 180. In addition, the domain dimensions, non-dimensionalised by  $\delta$  are 5.63, 2 and

2.815 for the streamwise, wall-normal and spanwise directions respectively. Regarding the computational mesh, the smooth wall case lattice contains 196 grid points in the streamwise direction, 196 in the wall-normal direction and 140 in the spanwise direction. However, for the irregular roughness case the has to be finer, especially near the walls, to capture all the scales of motion that are generated due to the increased turbulence. Therefore, the number of grid points is 280 in the streamwise direction, 280 in the wall-normal direction and 140 in the spanwise direction. The parameters for the validation are summarized in Table 2.1

Researcher	$Re_\tau$	$L_x/\delta$	$L_y/\delta$	$L_z/\delta$	$N_x$	$N_y$	$N_z$
Kim et al.	180	5.63	2	2.815	196	196	140
Thakkar et al.	180	5.63	2	2.815	280	280	140

Table 2.1: Parameters of the two validation cases.  $x, y$  and  $z$  denote the streamwise, wall-normal and spanwise direction, respectively. Note that the number of grid points for Thakkar’s study is larger than Kim’s. The reason behind this is the need to capture all the scales of motion, since the channel has irregular roughness and therefore promotes turbulence.

Figures 2.6 and 2.7 demonstrate that the present results overlap with both Kim’s and Thakkar’s results regarding the mean velocity profiles. Therefore, since there is a good agreement between the current code and the literature results, the simulations for the cases of this thesis can take place.

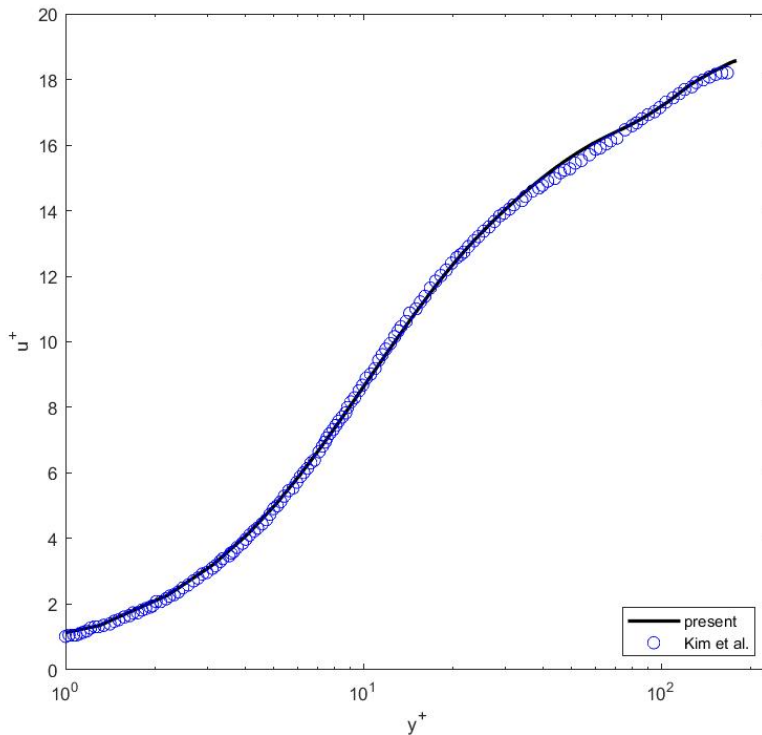


Figure 2.5: Validation of the present code with Kim’s simulation of a channel with smooth walls. As observed, there is a great agreement between Kim’s results and the current code.

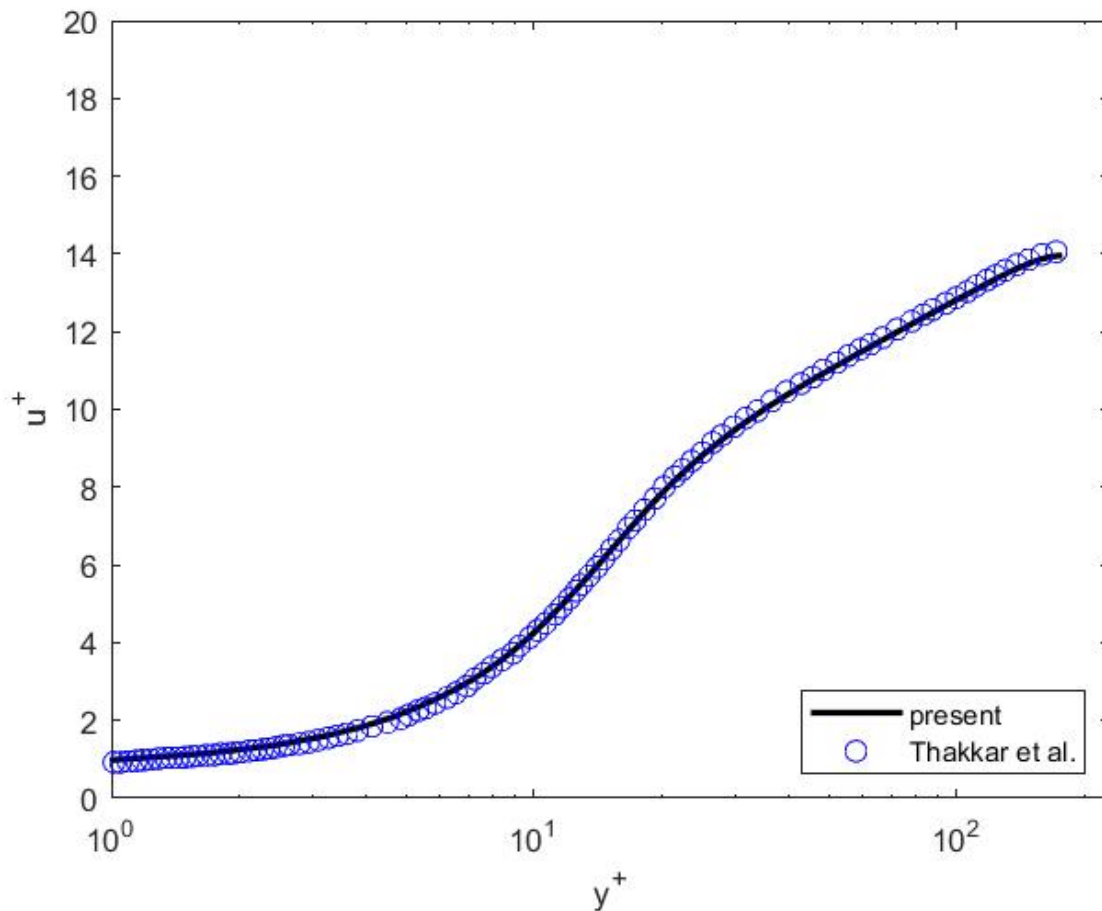


Figure 2.6: Validation of the present code with Thakkar's simulation of a channel with irregular rough walls. As observed, there is a great agreement between Thakkar's results and the current code.

## 2.7. Simulations-Geometry

Six different simulations take place. Buoyancy and roughness geometry are the two main variables that characterize each simulation. Regarding the aspect of buoyancy, the Richardson number takes the values of 0 and -0.8. In other words,  $Ri = 0$  means that the flow has zero buoyancy and  $Ri = -0.8$  means that the forced and natural convection are aligned and therefore the flow becomes buoyancy-aided. On the other hand the roughness geometry is distinguished between three cases. A case of a smooth wall, a case of a sinusoidal roughness with the direction of travel being in the streamwise direction, parallel to the flow (Figures 2.8 and 2.9) and a case with the same sinusoidal shape but the direction of travel being in the spanwise direction, normal to the flow (Figures 2.10 and 2.11).

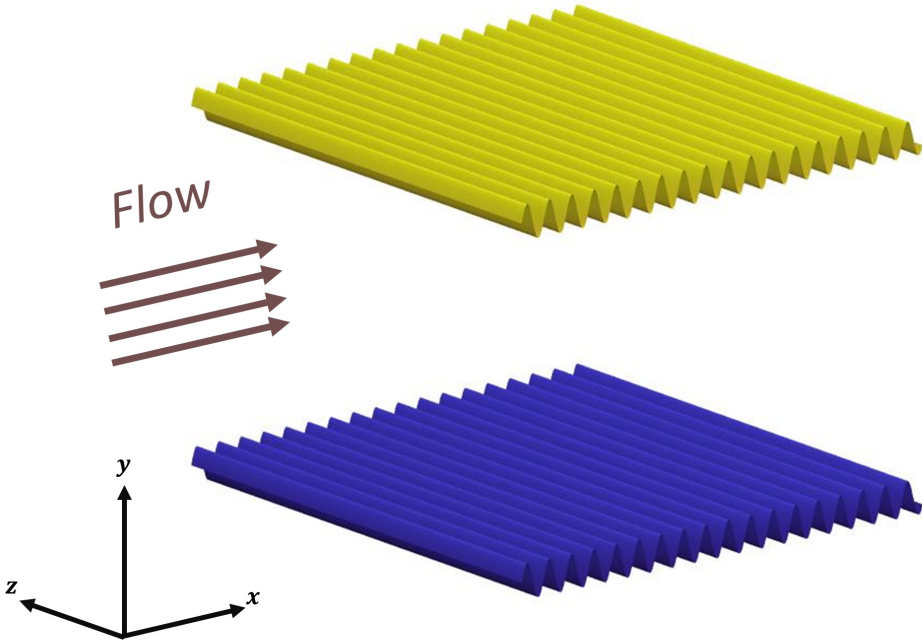


Figure 2.7: 3D view of the sinusoidal roughness with the direction of travel being in the streamwise direction, parallel to the flow.

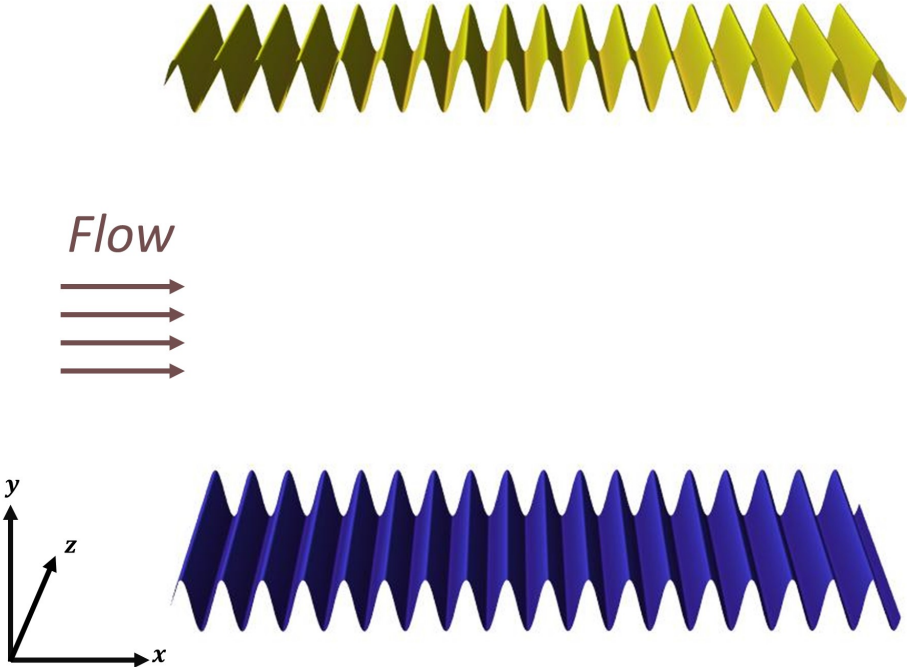


Figure 2.8: Different angle of view of the sinusoidal roughness with the direction of travel being in the streamwise direction, parallel to the flow.

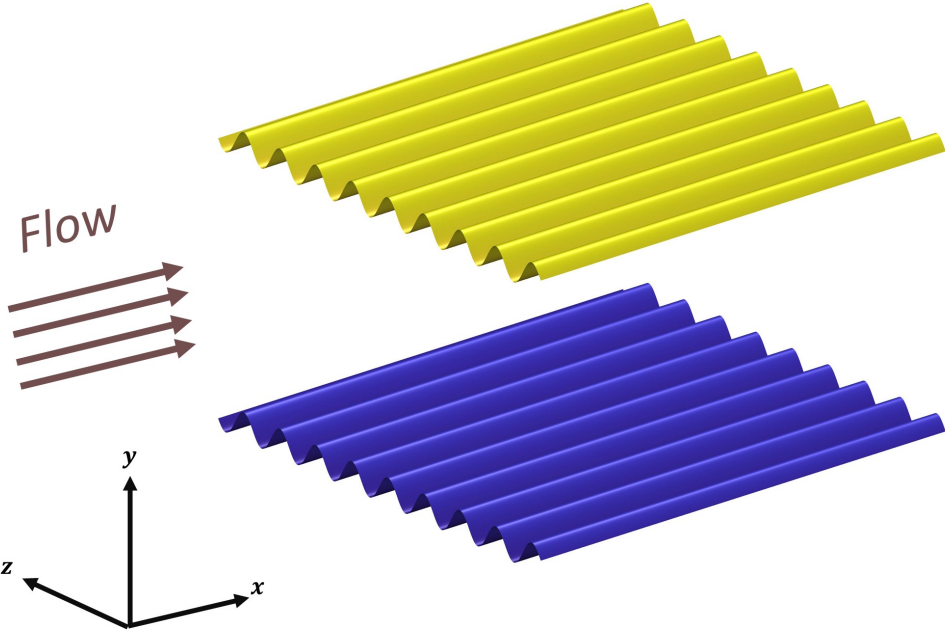


Figure 2.9: 3D view of the sinusoidal roughness with the direction of travel being in the spanwise direction, normal to the flow.



Figure 2.10: Different angle of view of the sinusoidal roughness with the direction of travel being in the spanwise direction, normal to the flow.

The function by which the roughness is constructed in the streamwise direction is:

$$y = 0.1 \sin\left(20\left(\frac{2\pi x}{5.63}\right)\right) \quad (2.29)$$

meaning that there are 20 sin waves with the amplitude of 0.1, along the  $x$ -dimension which has a length of 5.63.

Similarly, the function by which the roughness is constructed in the spanwise direction is:

$$y = 0.1 \sin\left(10\left(\frac{2\pi z}{2.815}\right)\right) \quad (2.30)$$

meaning that there are 10 sin waves with the amplitude of 0.1, along the  $z$ -dimension which has a length of 2.815.

The reason behind the choice of a sinusoidal shape of roughness is the fact that many industrial applications use square fins or grooves as a heat transfer augmentation technique. However, the current code is not suited for square shapes, thus the geometry is simplified by smoothing the square fins to sinusoidal shape fins. In addition, the literature contains rough surfaces similar to the current geometry. For example, Maas and Schumann investigated the impact of a wavy surface on turbulent flow by direct numerical simulations (Figure 2.12) [38]. Likewise, Cherukat et al. examined the turbulent flow over a sinusoidal solid wave surface by a direct numerical simulation [13]. Therefore, the current thesis can provide useful insights regarding the heat transfer aspect to the previous literature.

As already mentioned in the introduction, buoyancy can drastically affect the flow. Buoyancy-opposed flows induce turbulence and therefore heat transfer is augmented. On the other hand, buoyancy-aided flows promote laminarization, causing heat transfer deterioration. As described previously, the focus of this study is mainly on zero-buoyancy and buoyancy-aided flows, since the literature contains many buoyancy-opposed flows and less aided cases. It should be noted that the effect of buoyancy should be taken into consideration only when the density differences of the fluid are important, depending mainly on the fluid. Therefore, the present study covers both scenarios.

In conclusion, the results will give an insight on how the two types of regular roughness affect the heat transfer, when there is no buoyancy and when the flow is buoyancy-aided.

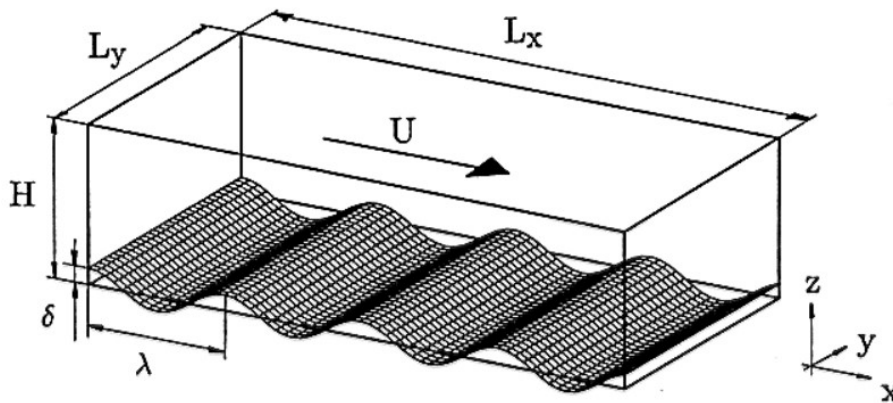


Figure 2.11: Flow configuration and geometry by Maas and Schumann [38].

## 2.8. Mesh

Simulation	$N_x$	$N_y$	$N_z$
Smooth $Ri = 0$	196	196	140
Smooth $Ri = -0.8$	196	196	140
Streamwise Roughness $Ri = 0$	280	280	140
Streamwise Roughness $Ri = -0.8$	280	280	140
Spanwise Roughness $Ri = 0$	280	280	140
Spanwise Roughness $Ri = -0.8$	280	280	140

Table 2.2: Number of grid points in each direction.  $x, y$  and  $z$  denote the streamwise, wall-normal and spanwise direction, respectively.

Table 2.2 summarizes the number of grid points in each direction. Note that for the cases where the walls are rough, the mesh is finer compared to the smooth wall cases. The reason behind this is the fact that the roughness of the wall is expected to induce turbulence to the flow. Therefore, in order to portray both the macro and micro structure of the flow, more grids are added to the mesh. Moreover, in the literature it is stated that buoyancy-aided flows promote laminarization. Consequently, one could argue that the simulations with  $Ri = -0.8$  are expected to display less turbulence than the zero-buoyancy cases and thus the mesh could be coarser. However, it is chosen to stay as it is in case where laminarization eventually is not promoted.

## 2.9. Boundary Conditions

Periodic boundary conditions are used for all the simulations. Having periodic boundary conditions decrease the size of the domain and therefore the number of grid points. Regarding the initial conditions, to this point they don't matter since the simulations run until the initial conditions are diffused out of the system and thus the flow reaches a steady state. The top and bottom walls which are the only rough walls, are kept cool with  $\theta_w = 0$ , while the bulk of fluid is heated volumetrically. Finally, Reynolds and Prandtl numbers are kept constant at 5500 and 1 respectively.

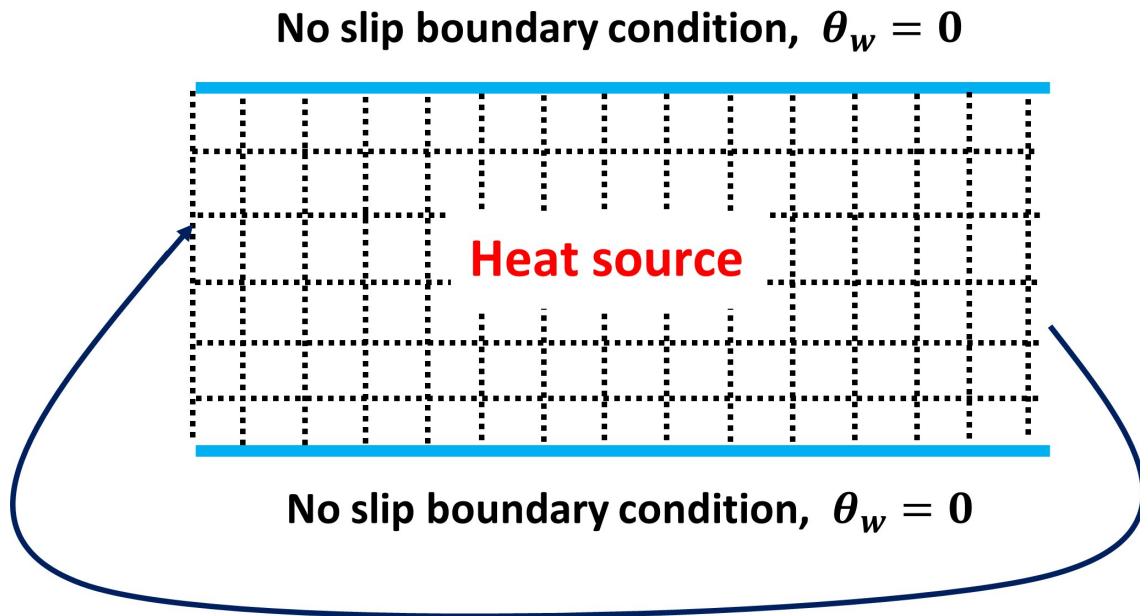


Figure 2.12: Schematic of the smooth wall domain with boundary conditions. The walls are kept cool with  $\theta_w = 0$ , while the bulk of fluid is heated volumetrically. Periodic boundary conditions are used for the inlet and outlet.

# 3

## Results-Discussion

Six simulations are performed; smooth walls, rough walls with streamwise orientation and rough walls with spanwise orientation is the one variable while zero-buoyancy and aided-buoyancy is the other. The variables of interest in this study are the mean velocity, the mean temperature, the mean Reynolds stresses, the mean turbulent heat flux and the Nusselt number for each case. These variables are examined through the wall normal distance for half the height of the channel. Figure 3.1 indicates the starting point ( $y/h=0$ ) and the ending point ( $y/h=1$ , middle of the channel) of the wall normal distance, on which the variables are examined for the smooth wall cases. Finally, the domain for the rough wall cases extends to  $y/h=-0.1$  (Figure 3.2).

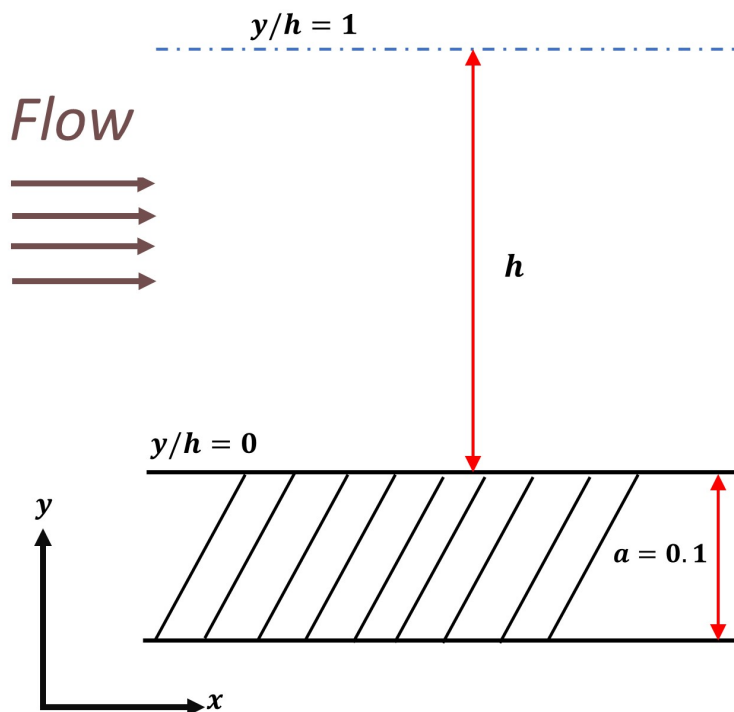


Figure 3.1: Schematic of the geometry for the smooth wall case.  $y/h=0$  is the starting point and  $y/h=1$  indicates the ending point and the middle of the channel as well.

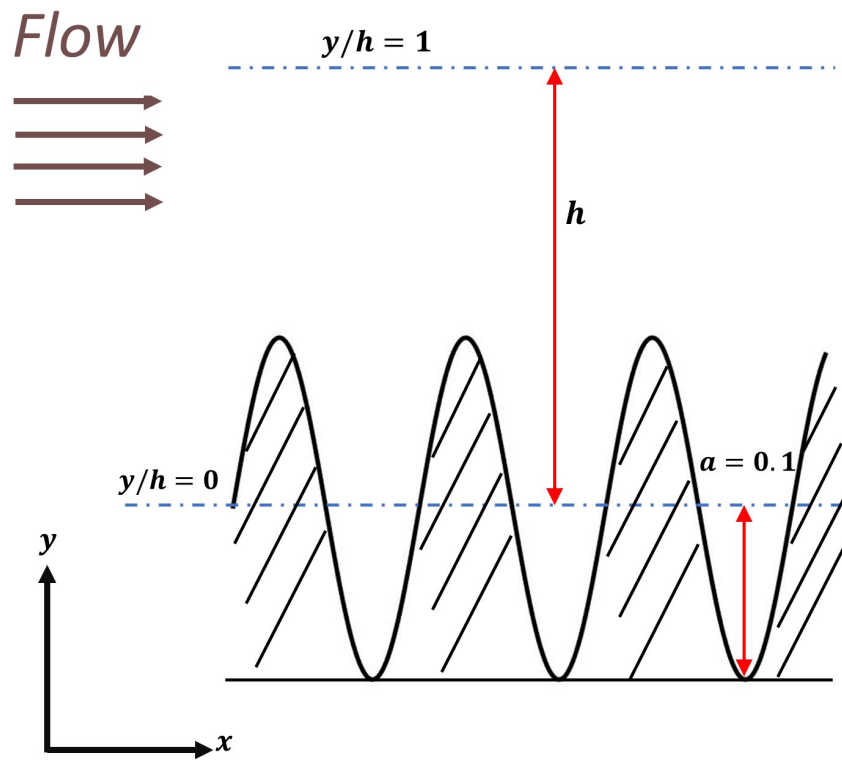


Figure 3.2: Schematic of the geometry for the streamwise roughness.  $y/h = -0.1$  is the starting point and  $y/h = 1$  indicates the ending point and the middle of the channel as well.

### 3.1. Smooth VS Streamwise, Ri=0

Figures 3.3 to 3.6 show how the sinusoidal streamwise roughness affects the flow, compared to the smooth wall case when there are no buoyancy effects. At first sight, it can be clearly observed in all of the figures, that the streamwise roughness (blue) produces a quite alternative profile for all the variables of interest, comparatively to the smooth wall case (black).

Figure 3.3 displays the velocity profile for both cases. Specifically, from  $y/h=0$  to  $y/h=0.05$ , the streamwise roughness model predicts negative values of the velocity flow field. These negative values occur due to the recirculation zones that are generated near the wall (Figure 3.7). Recirculation zones can be explained as a significant reversal of the flow (indicated by the green fluid inside the black box) in turbulent flows near a rough wall, which is due to the adverse pressure gradient [9]. As it is indicated by Figure 3.3, for  $y/h < 0.25$  the streamwise roughness case develops lower velocity values, than the smooth wall case. This is due to the recirculation zones which exist near the rough walls, in contrast to the smooth wall case in which no flow reversal zones are generated. However, for  $y/h > 0.25$  the streamwise orientation predicts higher velocity values compared to the smooth wall case, since the effect of the recirculation zones is impaired and the mass flow rate has to stay constant to conserve the momentum.

Figure 3.4 presents the Reynolds stresses for the streamwise roughness (blue) and the smooth wall case (black). In general, the Reynolds stresses represent an indication for the magnitude of turbulence of the flow. This means that high Reynolds stresses imply a great mixing of the flow, thus heat transfer improvement. Comparing the two curves, the Reynolds stresses of the streamwise roughness are much larger than the Reynolds stresses of the smooth wall case. Therefore, it is expected that heat transfer is augmented. Yet again, the change from positive to negative values for the streamwise case is a consequence of the recirculation zones, which exist near the wall. Remarkable is the fact that for  $y/h=1$ , which corresponds to the center of the channel, the Reynolds stresses for both cases decrease to zero, meaning there is no production of turbulence. This agrees pretty well with the velocity profile for both cases (Figure 3.3), as near the center the profile becomes flat and thus the gradient of the velocity with respect to the wall normal distance  $du/d(y/h)$  is zero.

The turbulent heat flux has a similar behavior to the Reynolds stresses and it can be correlated to the Nusselt number (ratio of convective to conducting heat transfer) which is discussed later. As can be seen in Figure 3.5, the magnitude of the turbulent heat flux for the streamwise roughness (blue) is much larger than the magnitude of the smooth wall case (black). This indicates the fact that the heat transfer of the streamwise roughness is much more powerful. Moreover, there is an agreement with the Reynolds stresses graph which shows that mixing of the flow is improved, thus heat transfer is magnified. In addition, analogously to the Reynolds stresses, the turbulent heat flux also decreases to zero at the center of the channel ( $y/h=1$ ).

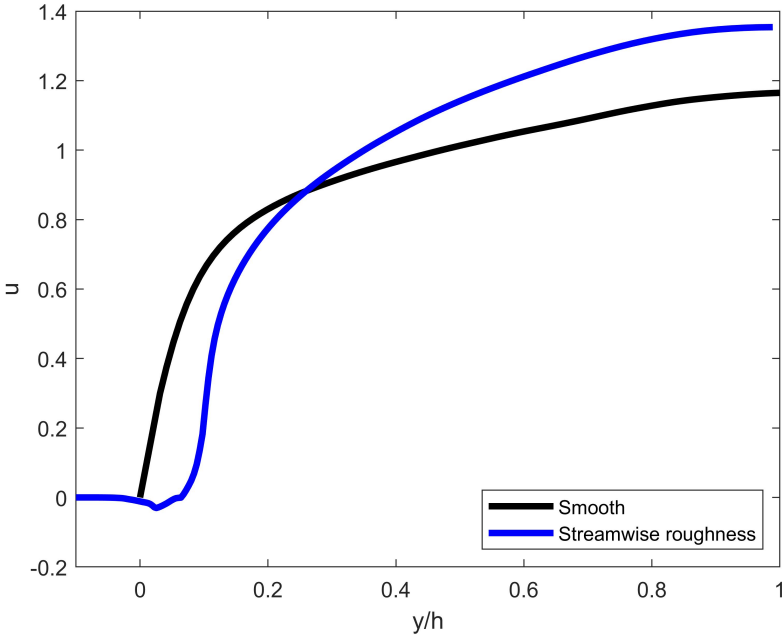


Figure 3.3: Velocity profile for the smooth wall and the streamwise roughness cases, when there is zero buoyancy.

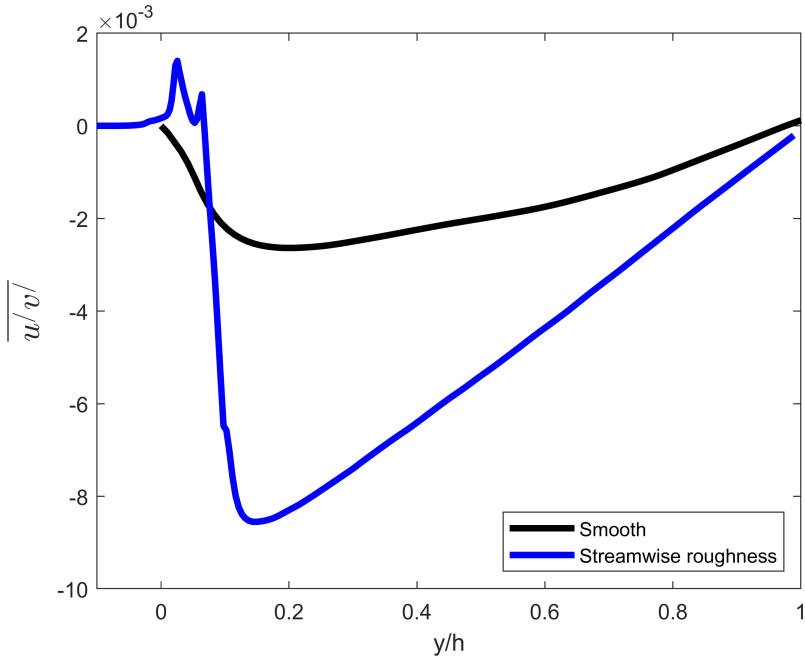


Figure 3.4: Reynolds stresses profile for the smooth wall and the streamwise roughness cases, when there is zero buoyancy.

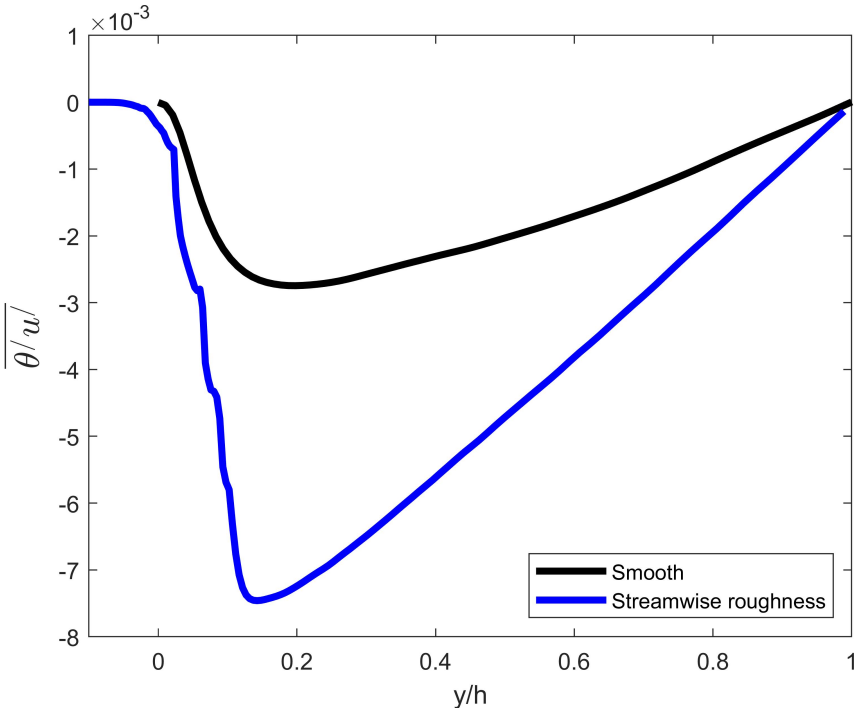


Figure 3.5: Turbulent heat flux profile for the smooth wall and the streamwise roughness cases, when there is zero buoyancy.

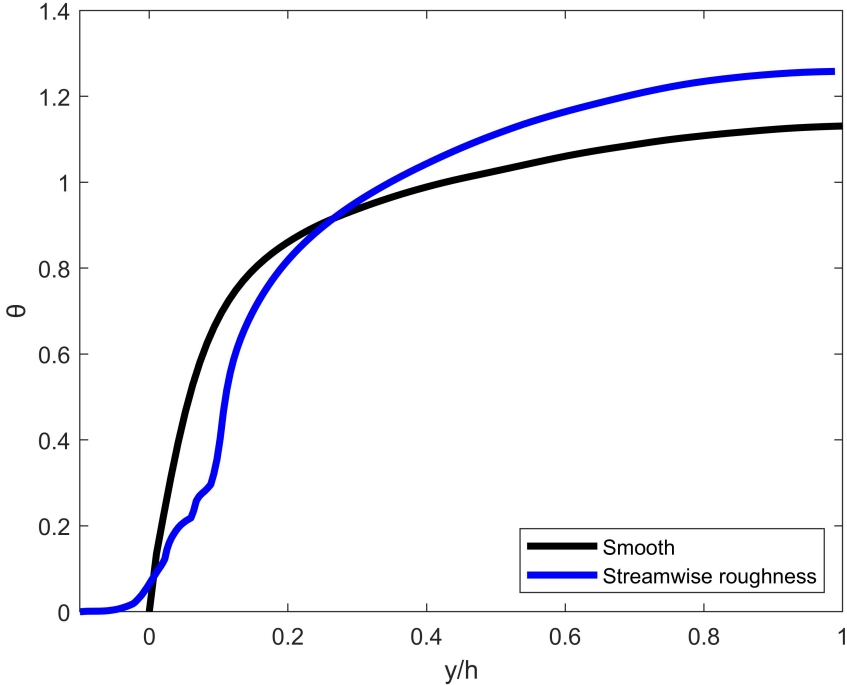


Figure 3.6: Temperature profile for the smooth wall and the streamwise roughness cases, when there is zero buoyancy.

Finally, Figure 3.6 indicates how the temperature field is affected by the two different types of surfaces. The results display that for  $y/h < 0.25$  the streamwise roughness model predicts a lower temperature profile than the smooth wall case. However, for  $y/h > 0.25$  the streamwise roughness develops higher temperature values, compared to the smooth wall scenario. This can be justified by the fact that for  $y/h < 0.25$  the Reynolds stresses reach their maxima, denoting a high production of turbulence, thus the mixing is finer. In addition, the turbulent heat flux is also at its peak in that region, meaning again that heat transfer is augmented. Recirculation zones are also present near the wall, which is something that should be taken into account. Therefore, these three facts can explain well the decreased temperature of the streamwise roughness case for  $y/h < 0.25$ . On the other hand, due to the heat source term  $\Phi$  which is discussed in Chapter 2 and the energy conservation law, the streamwise roughness case develops larger temperatures than the smooth wall case, for  $y/h > 0.25$ . This behavior is analogous to the velocity profile in which momentum has to be conserved.

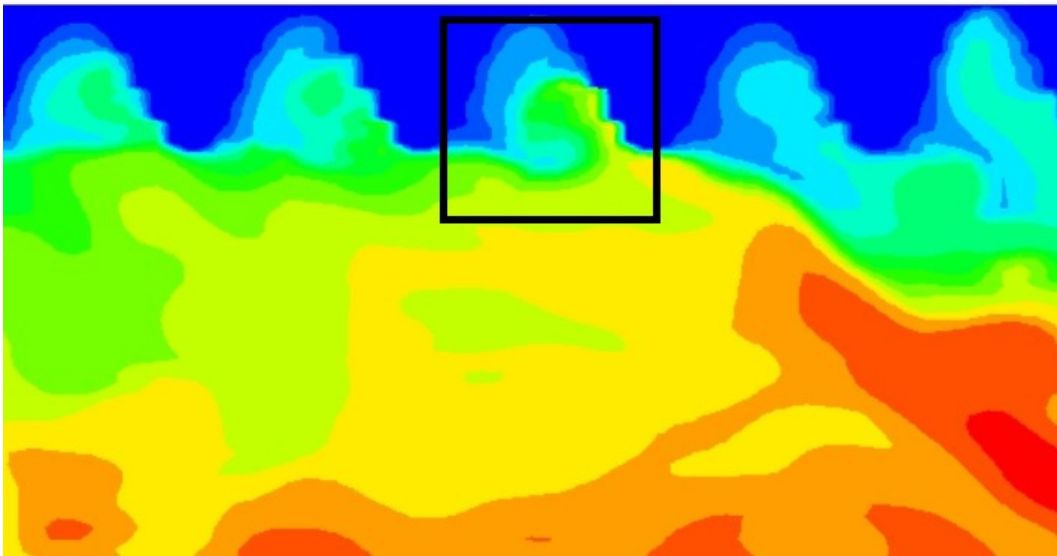


Figure 3.7: Recirculation zones are generated near the wall for the streamwise roughness case. This phenomenon can be explained as a significant reversal of the flow (denoted by the green fluid inside the black box), as a result of the adverse pressure gradient.

## 3.2. Smooth VS Spanwise, Ri=0

Figures 3.8 to 3.11 present the impact of the sinusoidal spanwise roughness on the flow, compared to the smooth wall case when there is zero-buoyancy. Similarly to the streamwise direction, the spanwise roughness model (red) predicts a different profile for the variables of interest, compared the smooth wall case (black).

Beginning with Figure 3.8, the velocity profiles for both scenarios are presented. It can be seen that for  $y/h < 0.175$  the smooth wall model predicts larger magnitude for the velocity, but for  $y/h > 0.175$  the spanwise roughness velocity profile overcomes the smooth wall one. This again can be justified by the fact that roughness delays the flow near the walls and therefore the velocity near the middle of the channel increases to conserve momentum.

Moving on to Figure 3.9, the Reynolds stresses are displayed. Comparing the two curves, for  $y/h < 0.7$  the Reynolds stresses for the spanwise roughness have greater values than the smooth wall case. This indicates that the former one has a better mixing of the flow than the latter one, thus increasing the overall heat transfer. However, for  $y/h > 0.7$  both curves have the same value. Once more, it should be noted that for  $y/h = 1$ , which corresponds to the center of the channel, the Reynolds stresses for both cases reduce to zero, meaning there is no production of turbulence. This agrees quite good with the velocity profile of both cases (Figure 3.8), as near the center the profile becomes flat and thus the gradient of the velocity with respect to the wall normal distance ( $du/d(y/h)$ ) is zero.

Analogous result to the Reynolds stresses has the turbulent heat flux. As it can be seen in Figure 3.10, the magnitude of the turbulent heat flux for the spanwise roughness (red) is much higher than that for the smooth wall case (black). This points out that the heat transfer of the spanwise orientation is stronger and also corresponds to the Reynolds stresses graph which presents that turbulence is induced, thus the mixing of the flow is improved.

Finally, Figure 3.11 displays how the temperature field is affected by the two different types of surfaces. The results show that for  $y/h < 0.2$  the spanwise roughness model predicts a lower temperature profile than the smooth wall case. However, for  $y/h > 0.2$  the spanwise roughness develops larger temperatures, compared to the smooth wall one. This is similar to the temperature profile of the streamwise orientation. Particularly, in the region of  $y/h < 0.25$ , the Reynolds stresses reach their maxima implying a fine mixing. In addition, the turbulent heat flux is also at its peak. Both phenomena denote heat transfer improvement for the spanwise orientation and for this reason the temperature values of the smooth wall case are larger. However, for  $y/h > 0.25$  the spanwise case predicts greater temperature values than the smooth wall case, since the heat source term  $\Phi$  provides heat to the flow and energy has to be conserved. Once more this behaviour is analogous to the velocity profile in which momentum is conserved.

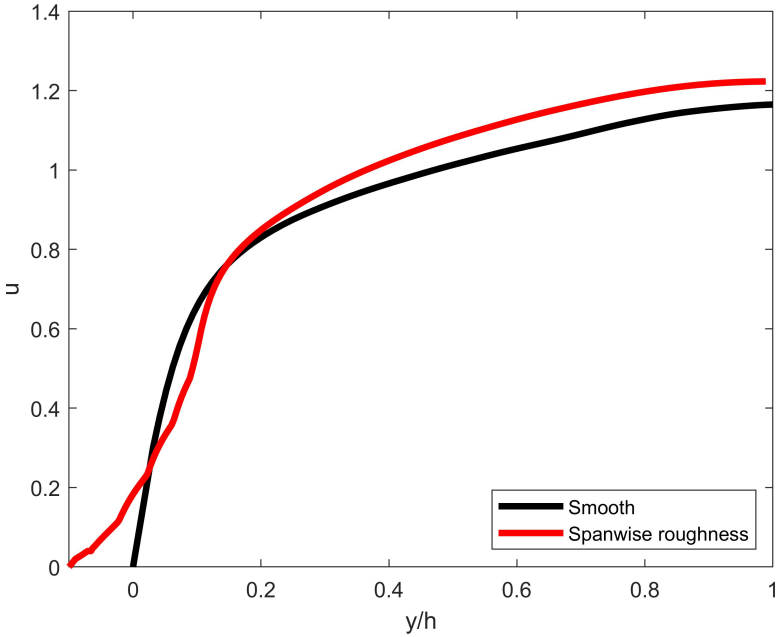


Figure 3.8: Velocity profile for the smooth wall and the spanwise roughness cases, when there is zero buoyancy.

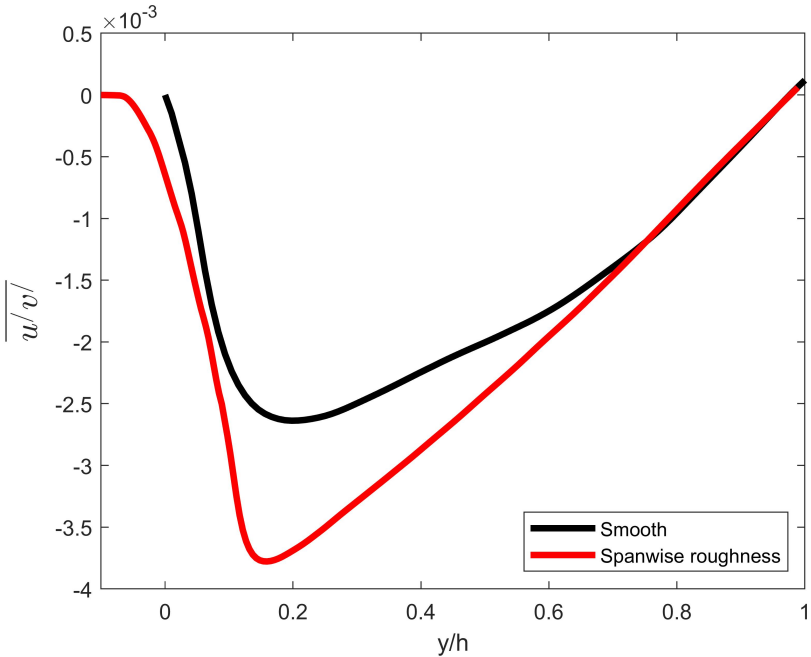


Figure 3.9: Reynolds stresses profile for the smooth wall and the spanwise roughness cases, when there is zero buoyancy.

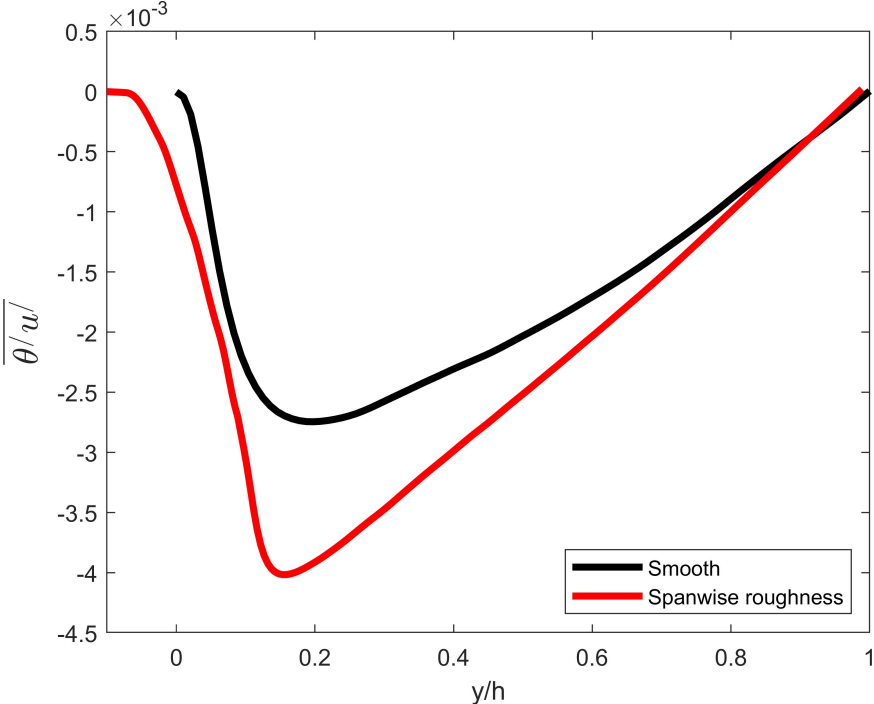


Figure 3.10: Turbulent heat flux profile for the smooth wall and the spanwise roughness cases, when there is zero buoyancy.

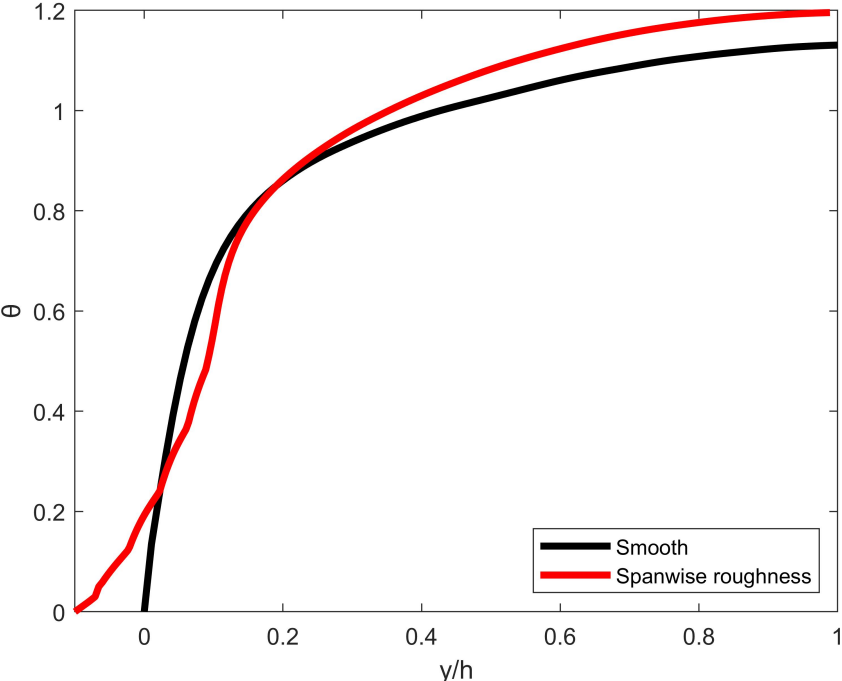


Figure 3.11: Temperature profile for the smooth wall and the spanwise roughness cases, when there is zero buoyancy.

### 3.3. Smooth VS Streamwise, Ri=-0.8

Figures 3.12 to 3.15 show how the sinusoidal streamwise roughness affects the flow, compared to the smooth wall case when the flow is buoyancy-aided. Certainly, the streamwise roughness model (blue) creates velocity, temperature, Reynolds stresses and turbulent heat flux profiles with distinct differences, when compared to the smooth wall case.

Figure 3.12 displays the velocity profile for both cases. Both curves clearly indicate the formation of the "M" shape velocity profile. In other words, buoyancy forces are aligned with the flow and since buoyancy is taken into account, the velocity near the wall is increased. However, near the center of the channel the values are diminishing, thus resulting in the "M" shape velocity profile. Regarding the streamwise roughness, for  $y/h < 0.075$  the values drop below zero indicating again the presence of the recirculation zones. Once more, the recirculation zones have an impact on the flow by maintaining the velocity magnitude of the streamwise roughness low ( $y/h < 0.15$ ), compared with the smooth wall case in which no flow reversal zones are generated. However, from  $y/h > 0.15$ , the streamwise roughness develops a higher value for the velocity profile than the smooth wall case, since the effect of the recirculation zones is impaired and the mass flow rate has to stay constant to conserve the momentum. Highly important is the velocity gradient of each curve which is strongly connected to the Reynolds stresses in Figure 3.13. It can be observed that after the two curves reach their maximum values, the velocity gradient (or slope) of the streamwise roughness is greater than the smooth wall one. This leads to the conclusion that the Reynolds stresses of the streamwise roughness in that area are expected to be larger and therefore the mixing of the flow is improved. Analogously, the Reynolds stresses for the smooth wall case are expected to be larger between  $y/h = 0.2$  and  $y/h = 0.25$ , since the velocity profile of the streamwise roughness reaches its maximum and therefore the velocity gradient is zero.

Figure 3.13 presents the Reynolds stresses for the streamwise roughness (blue) and the smooth wall case (black). To begin with, the change from positive to negative values for the streamwise case really close to the wall ( $y/h < 0.075$ ), is once more a result of the recirculation zones, which exist in that area. However, both curves are flipped compared to the zero-buoyancy case due to the "M" shape of the velocity profile. Specifically, the velocity gradient becomes negative, thus making the Reynolds stresses positive. It can also be observed that when the velocity profiles for both surfaces reach their maximum value (when  $du/d(y/h) = 0$ ), the Reynolds stresses are equal to zero ( $y/h = 0.215$  for the streamwise roughness and  $y/h = 0.1$  for the smooth wall case). In addition, the magnitudes of the Reynolds stresses agree pretty well with the velocity gradients in Figure 3.12. Simply put, for  $0.2 < y/h < 0.25$  the smooth wall case has higher Reynolds stresses since its velocity gradient is larger compared to the streamwise roughness. On the other hand, for the rest of the channel, the streamwise orientation presents higher Reynolds stresses as a result of the steeper velocity shifts. Finally, for  $y/h = 1$ , which corresponds to the center of the channel, the Reynolds stresses for both cases decrease to zero, meaning there is no production of turbulence.

Figure 3.14 shows the turbulent heat flux for both scenarios. Once more, the values of the turbulent heat flux for the streamwise roughness are much higher than those for the smooth wall case. This again indicates the fact that heat transfer is improved for the streamwise direction related to the smooth wall case. It also does not conflict with

the Reynolds stresses which show high production of turbulent kinetic energy for the streamwise roughness and therefore better mixing.

Finally, Figure 3.15 indicates how the temperature field is affected by the two different types of surfaces. The results display that for  $y/h < 0.215$  the streamwise roughness model predicts a lower temperature profile than the smooth wall case. However, for  $y/h > 0.215$  the streamwise roughness develops higher temperature, compared to the smooth wall. Similarly to the zero-buoyancy case, one can justify the decreased temperature of the streamwise roughness for  $y/h < 0.215$  with the Reynolds stresses. In other words, the Reynolds stresses reach their maxima in that area, denoting that the production of turbulence is high, thus the mixing is finer. In addition, the turbulent heat flux is also at its peak in that region, meaning again that heat transfer is augmented. Recirculation zones are also present near the wall, which is something that should be considered. Therefore, these three statements can explain the decreased temperature of the streamwise roughness case for  $y/h < 0.215$ . On the other hand, due to the heat source term  $\Phi$  which is discussed in Chapter 2 and the energy conservation law, the streamwise roughness case develops larger temperatures than the smooth wall case, for  $y/h > 0.215$ . This behavior is analogous to the velocity profile in which momentum has to be conserved.

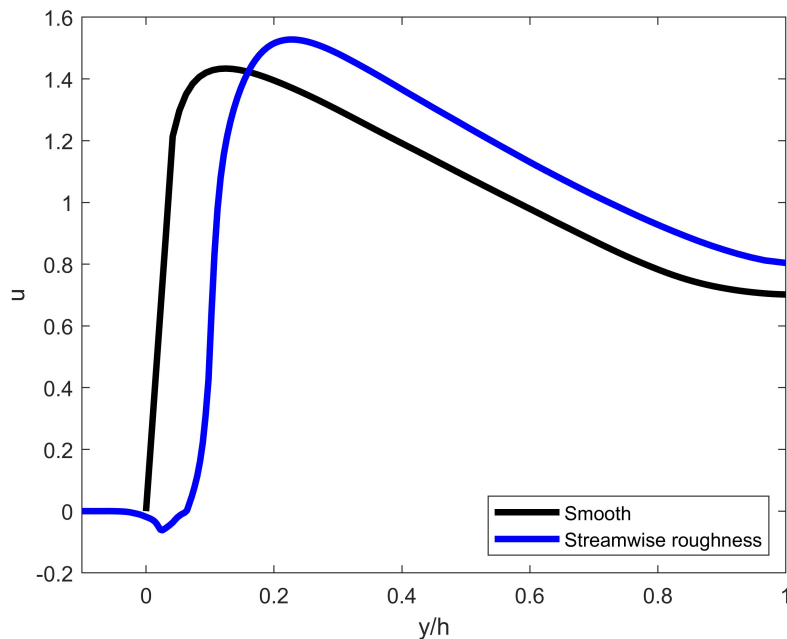


Figure 3.12: Velocity profile for the smooth wall and the streamwise roughness cases, when the flow is buoyancy-aided.

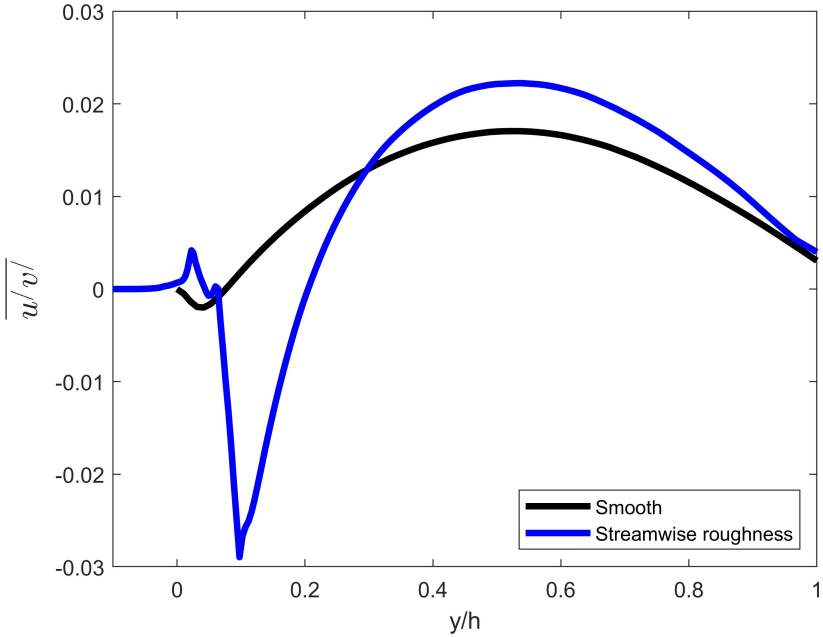


Figure 3.13: Reynolds stresses profile for the smooth wall and the streamwise roughness cases, when the flow is buoyancy-aided.

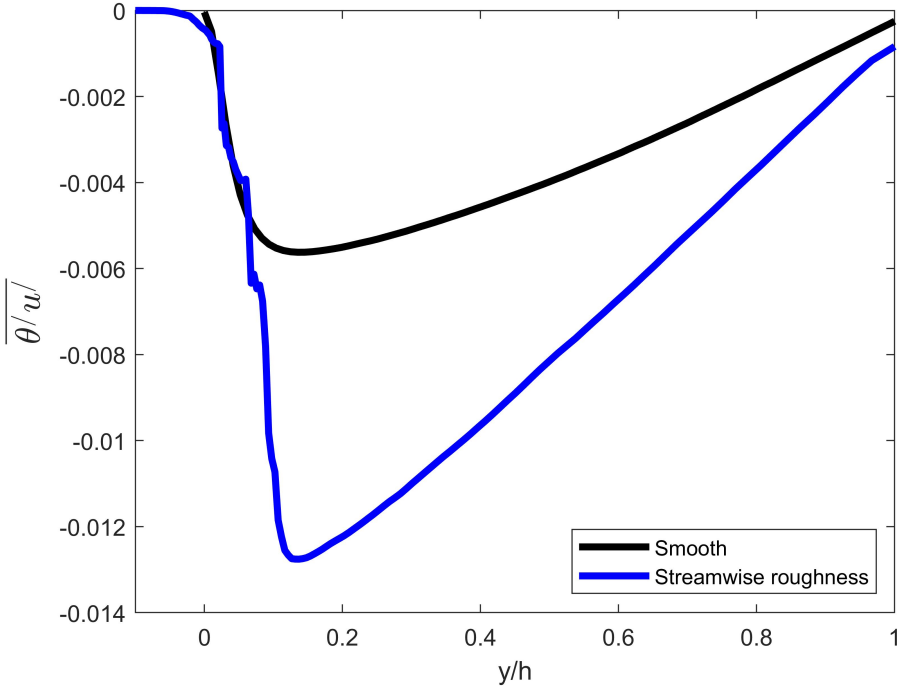


Figure 3.14: Turbulent heat flux profile for the smooth wall and the streamwise roughness cases, when the flow is buoyancy-aided.

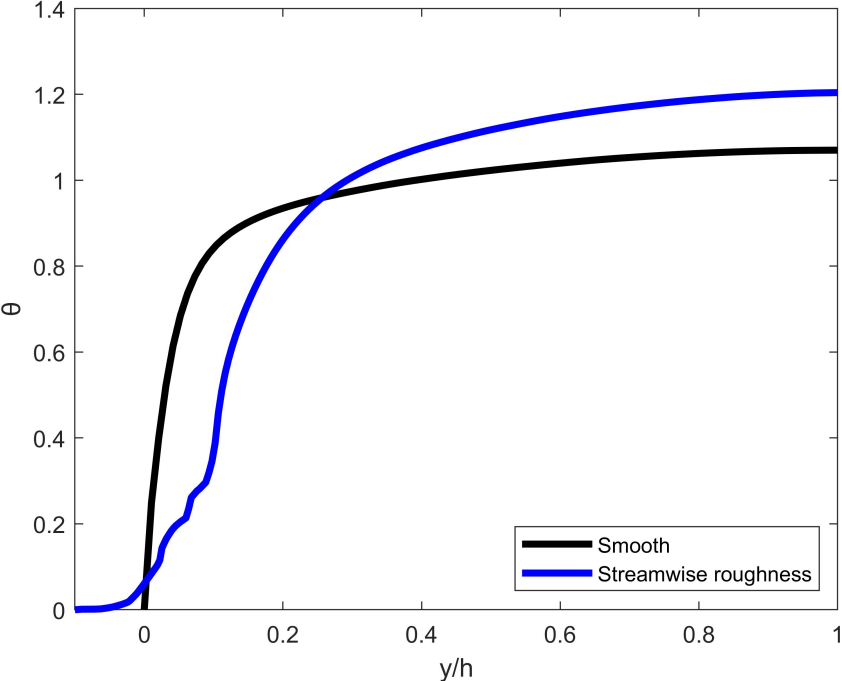


Figure 3.15: Temperature profile for the smooth wall and the streamwise roughness cases, when the flow is buoyancy-aided.

### 3.4. Smooth VS Spanwise, $Ri=-0.8$

Figures 3.16 to 3.19 present the impact of the sinusoidal spanwise roughness on the flow, compared to the smooth wall case when the flow is buoyancy-aided. Once more, the spanwise roughness model (red) predicts a different profile for all the variables of interest, in comparison with the smooth wall case (black).

Starting with Figure 3.16, the velocity profiles for both scenarios are presented. As it is shown, both profiles form the "M" shape which is also observed in the streamwise roughness as well. In particular, the velocity is increased near the wall due to the buoyancy effect and decreases near the center of the channel. Major remark on the velocity profiles are the gradients of each graph which are related to the Reynolds stresses in Figure 3.17. It can be observed that, after the two profiles reach their maximum values, the velocity gradient (or slope) of the spanwise roughness case is higher than the smooth wall one. As a result, the Reynolds stresses of the spanwise orientation in that area are expected to be larger, thus the mixing of the flow is anticipated to be finer.

Proceeding to Figure 3.17, the Reynolds stresses are displayed. Comparing the two curves, the spanwise roughness model predicts higher Reynolds stresses values than the smooth wall case for the whole half channel. This states that the former one has a finer mixing of the flow compared to the latter one, thus increasing the overall heat transfer. In addition, the magnitudes of the Reynolds stresses agree pretty well with the velocity gradients in Figure 3.16. Otherwise stated, the spanwise roughness has higher Reynolds stresses since its velocity gradient is higher compared to the smooth wall case. Another observation is the fact that even though both surfaces have the same shape for the velocity profile, their Reynolds stresses profiles are different. Specifically, the smooth wall case has negative Reynolds stresses for  $y/h < 0.1$ , then hits zero and then has only positive values. This agrees really well with the velocity profile, which increases for  $y/h < 0.1$  until it reaches its maximum value at  $y/h = 0.1$  and then decreases for the rest of the channel. On the other hand, the spanwise roughness has only positive Reynolds stresses.

Similar result to the Reynolds stresses has the turbulent heat flux. As it is presented in Figure 3.18, the values of the turbulent heat flux for the spanwise roughness (red) are much higher than those for the smooth wall case (black). This points out that the spanwise orientation has an enhanced heat transfer compared to the smooth wall case. In addition, it is in agreement with the Reynolds stresses graph which presents that turbulence is generated, thus the mixing of the flow is improved.

Finally, Figure 3.19 displays how the temperature field is affected by the two different types of surfaces. The results show that for  $y/h < 0.2$  the spanwise roughness model predicts a lower temperature profile than the smooth wall case. That is due to the fact that in the region of  $y/h < 0.25$ , the Reynolds stresses reach their maxima denoting a fine mixing and turbulent heat flux is also at its peak. Both phenomena indicate heat transfer improvement for the spanwise orientation and for this reason the temperature values of the smooth wall case are larger. However, for  $y/h > 0.2$  the spanwise roughness develops higher temperature, compared to the smooth wall case, since the heat source term  $\Phi$  provides heat to the flow and energy has to be conserved. Once more this behaviour is analogous to the velocity profile in which momentum is conserved.

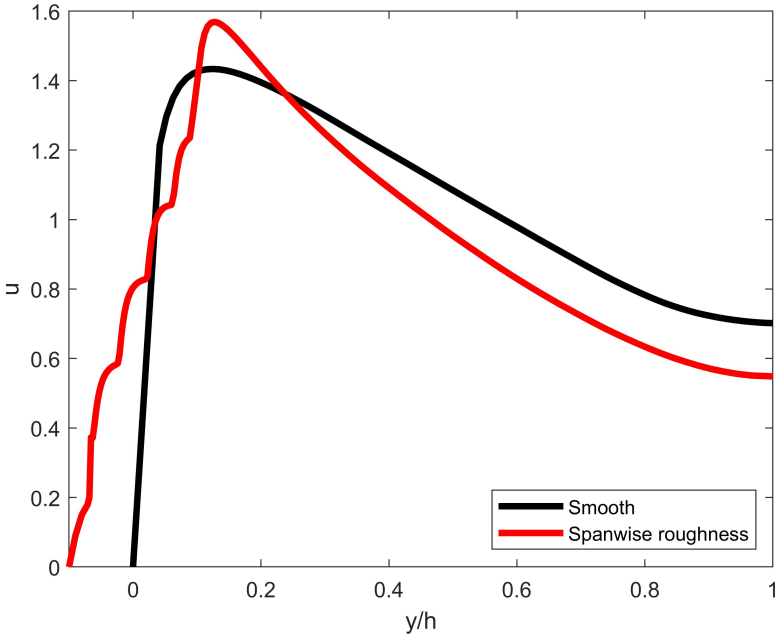


Figure 3.16: Velocity profile for the smooth wall and the spanwise roughness cases, when the flow is buoyancy-aided.

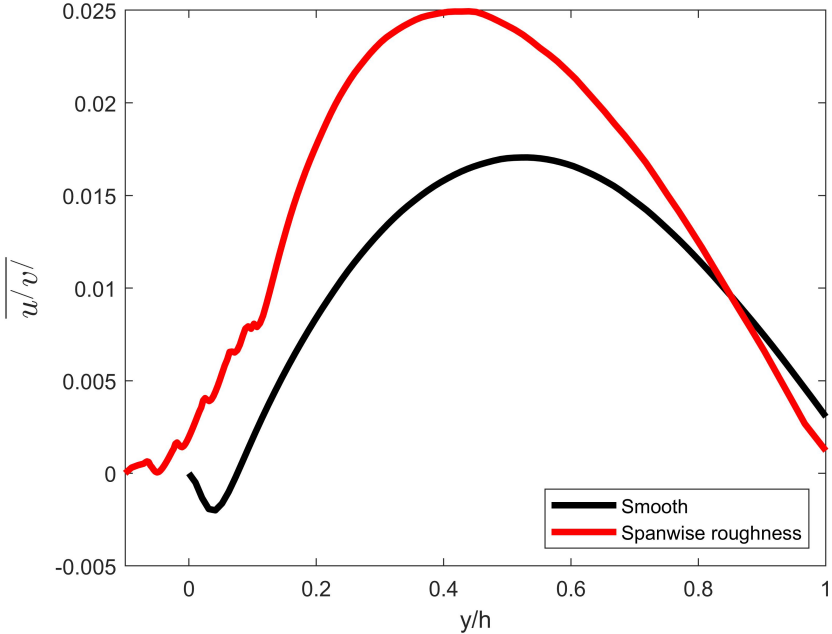


Figure 3.17: Reynolds stresses profile for the smooth wall and the spanwise roughness cases, when the flow is buoyancy-aided.

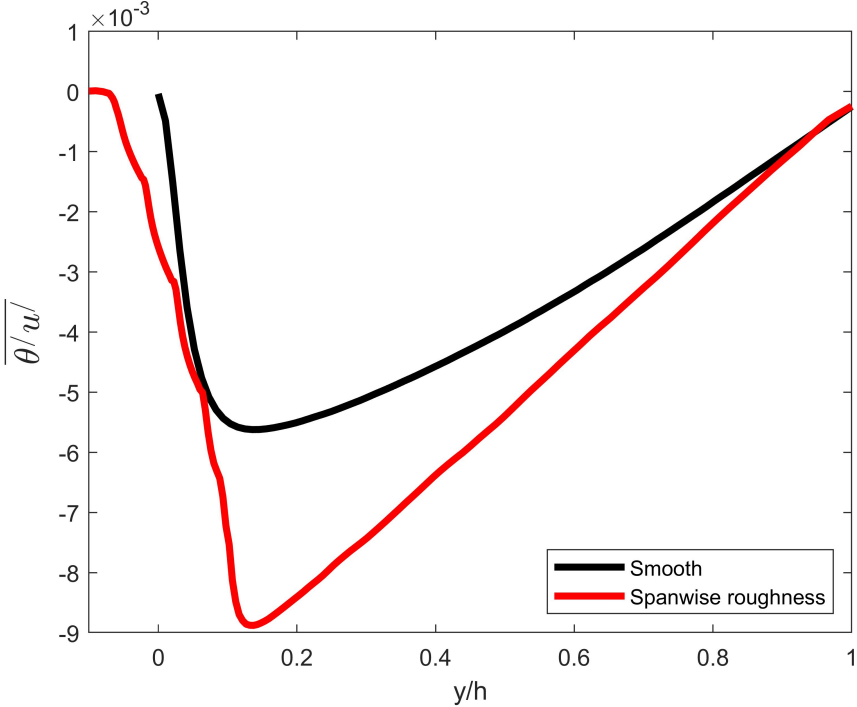


Figure 3.18: Turbulent heat flux profile for the smooth wall and the spanwise roughness cases, when the flow is buoyancy-aided.

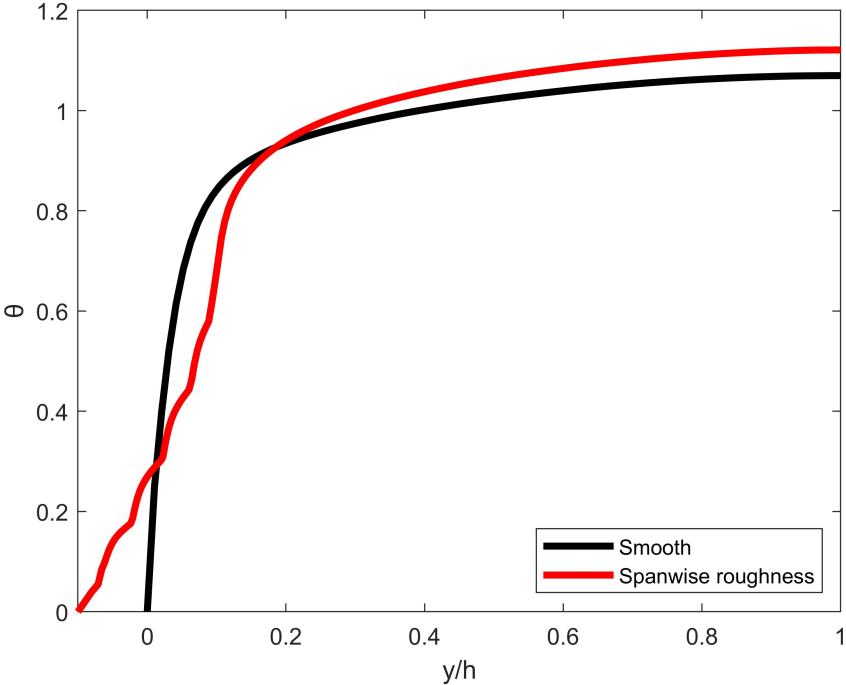


Figure 3.19: Temperature profile for the smooth wall and the spanwise roughness cases, when the flow is buoyancy-aided.

### 3.5. Streamwise roughness VS Spanwise roughness

Subsequently, the streamwise and spanwise surface roughness are compared to each other for both zero-buoyancy and buoyancy-aided flow. This comparison can give an insight on which roughness results in the best mixing and therefore the most enhanced heat transfer. In Figure 3.21, it is shown that in most of the region the streamwise roughness has higher Reynolds stresses than the spanwise orientation, for both buoyancy scenarios. Therefore, the mixing of the flow for the streamwise roughness can be considered as the best out of the two. Regarding the turbulent heat flux (Figure 3.22) once more, the streamwise roughness model anticipates greater values than the spanwise one. Consequently, it can be stated that the streamwise orientation has a more enhanced heat transfer rate compared to the spanwise case. In addition, the temperature profiles show that for  $y/h < 0.3$  the streamwise orientation predicts lower magnitude compared to the spanwise one, due to the recirculation zones. However, for  $y/h > 0.3$  the streamwise roughness case has a larger temperature magnitude, due to the heat source  $\Phi$  and the energy conservation law. Finally, Figure 3.20 indicates the presence of the recirculation zones for the streamwise roughness near the wall, in contrast to the spanwise orientation which does not have any flow reversal zones.

In conclusion, all the variables of study show that the streamwise roughness case has a better mixing and therefore an enhanced heat transfer compared to the spanwise orientation.

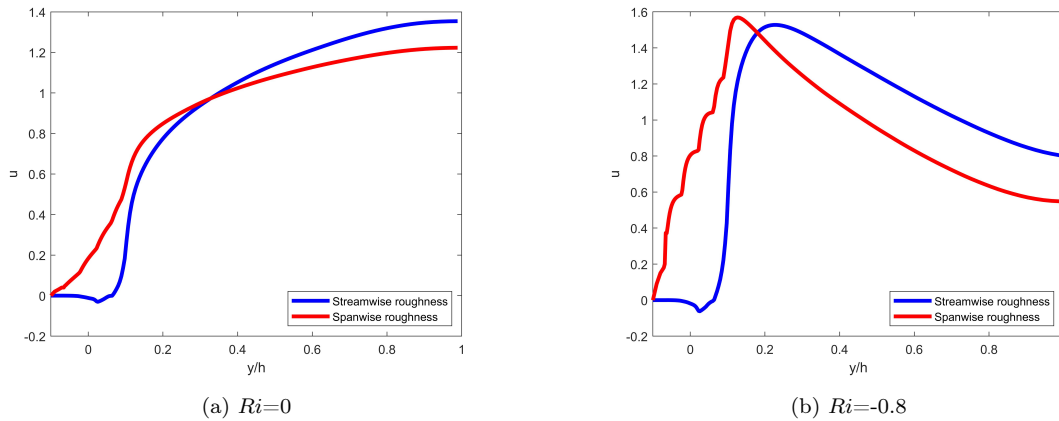


Figure 3.20: Velocity profile for the streamwise and spanwise roughness cases, when there is zero-buoyancy (left) and when the flow is buoyancy-aided (right).

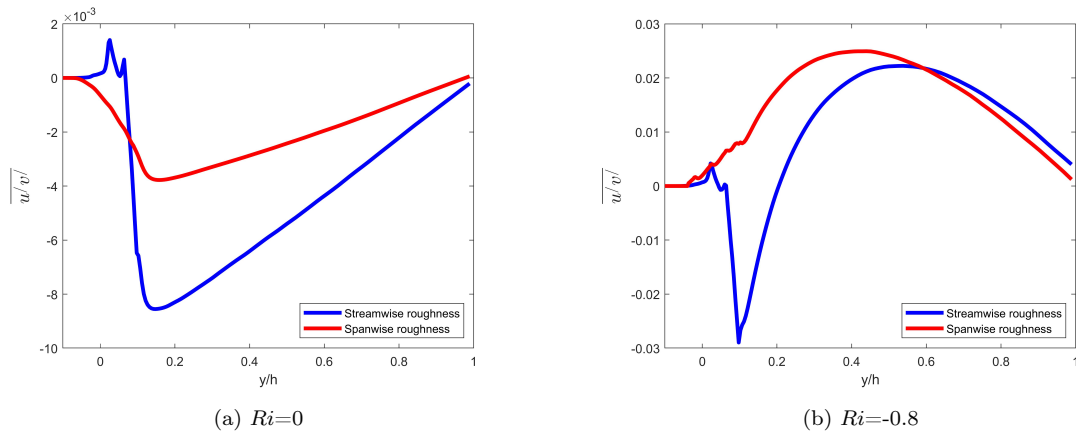


Figure 3.21: Reynolds stresses profile for the streamwise and spanwise roughness cases, when there is zero-buoyancy (left) and when the flow is buoyancy-aided (right).

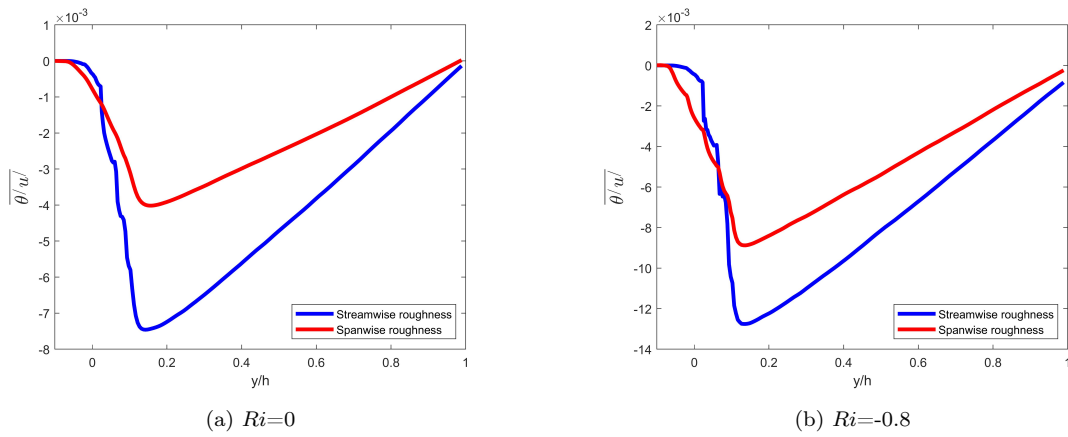


Figure 3.22: Turbulent heat flux profile for the streamwise and spanwise roughness cases, when there is zero-buoyancy (left) and when the flow is buoyancy-aided (right).

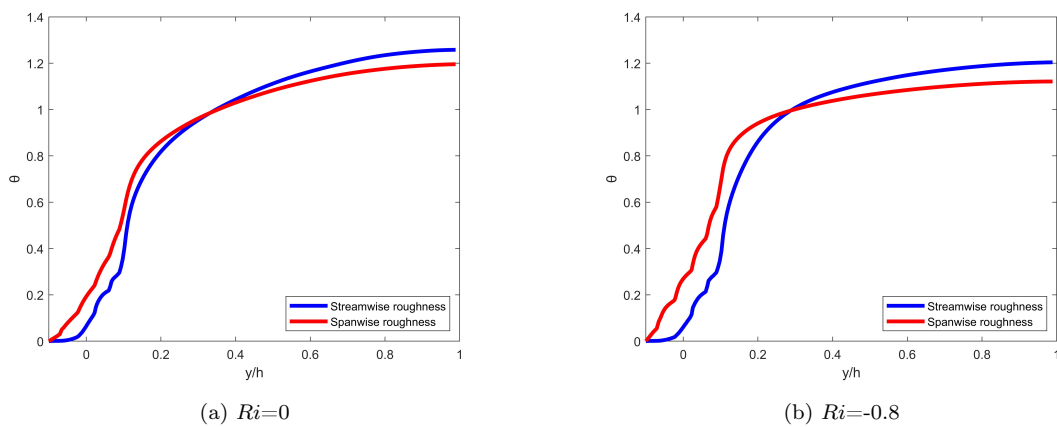


Figure 3.23: Temperature profile for the streamwise and spanwise roughness cases, when there is zero-buoyancy (left) and when the flow is buoyancy-aided (right).

### 3.6. Nusselt number calculation

For the calculation of the Nusselt number of each case a macro balance is constructed (Figure 3.24):

$$\rho C_p V \frac{dT}{dt} = q_1 L_y L_z - q_2 L_y L_z - q_3 L_x L_z - q_4 L_x L_z + \Phi L_x L_y L_z \quad (3.1)$$

where  $\rho$  is the density,  $C_p$  the specific heat capacity,  $V$  the volume,  $T$  the temperature and  $L_x$ ,  $L_y$ ,  $L_z$  the dimensions of the macrobalance. In addition,  $q_1$ ,  $q_2$ ,  $q_3$  and  $q_4$  are heat fluxes and  $\Phi$  is the volumetric heat source/sink that is explained in the Methodology part.

Having in mind that, the macrobalance is constructed when the flow reaches a steady state,  $q_1$  is equal to  $q_2$  due to the periodic boundary conditions and  $q_3$  is equal to  $q_4$  and equal to  $q_{wall}$  which represents the heat flux normal to the isothermal rough walls, Equation 3.1 reduces to:

$$q_{wall} = \frac{\Phi L_y}{2} \quad (3.2)$$

In addition, the convective heat transfer coefficient is calculated via:

$$h = \frac{q_{wall}}{T_b - T_{wall}} \quad (3.3)$$

and finally the Nusselt number is calculated using:

$$Nu = \frac{h \cdot 2\delta}{k} \quad (3.4)$$

where  $2\delta$  is the height of the channel and  $k$  is the thermal conductivity.

The simple method of the macrobalance is used to calculate the Nusselt numbers for the rough wall cases, since those geometries are complex. However, considering that the smooth surface is a much simpler geometry, the Nusselt numbers for the smooth wall cases are calculated by the Gnielinsky correlation for smooth walls [55]:

$$Nu = \frac{\frac{C_f}{2}(Re - 1000)Pr}{1 + 12.7\sqrt{\frac{C_f}{2}}(Pr^{\frac{2}{3}} - 1)} \left[ 1 + \left( \frac{d_h}{L} \right)^{\frac{1}{3}} \right] \left( \frac{Pr_m}{Pr_w} \right)^{0.11} \quad (3.5)$$

where  $d_h$  is the hydraulic diameter of the channel,  $Pr_m$  and  $Pr_w$  are the Prandtl numbers at the bulk and wall temperature respectively,  $L$  is the length of the channel and  $C_f$  is the friction factor given by Dean's correlation [16]:

$$C_f = 0.073Re^{-0.25} \quad (3.6)$$

Table 3.1 presents the Nusselt numbers for each simulation. Beginning with the zero-buoyancy scenario, clearly the roughness improve the Nusselt number and therefore the heat transfer as well. In particular, the streamwise roughness increases the Nusselt number by 163% while the spanwise roughness by 45%. It should also be noticed that the streamwise roughness is enhancing the Nusselt number approximately 1.8 times more than the spanwise roughness. The fact that streamwise roughness improves the heat transfer much more than the spanwise one, is also shown in the Reynolds stresses and

Simulation	Nusselt
Smooth $Ri = 0$	39.0
Streamwise $Ri = 0$	102.7
Spanwise $Ri = 0$	56.7
Smooth $Ri = -0.8$	67.4
Streamwise $Ri = -0.8$	167.7
Spanwise $Ri = -0.8$	116.9

Table 3.1: Nusselt number of each simulation based on the macrobalance method.

turbulent heat flux figures between the two roughness schemes. Regarding the buoyancy-aided case, the streamwise roughness increases the Nusselt number by 149% while the spanwise roughness by 74%. Once more the streamwise roughness increases the Nusselt number approximately 1.4 times more than the spanwise roughness.

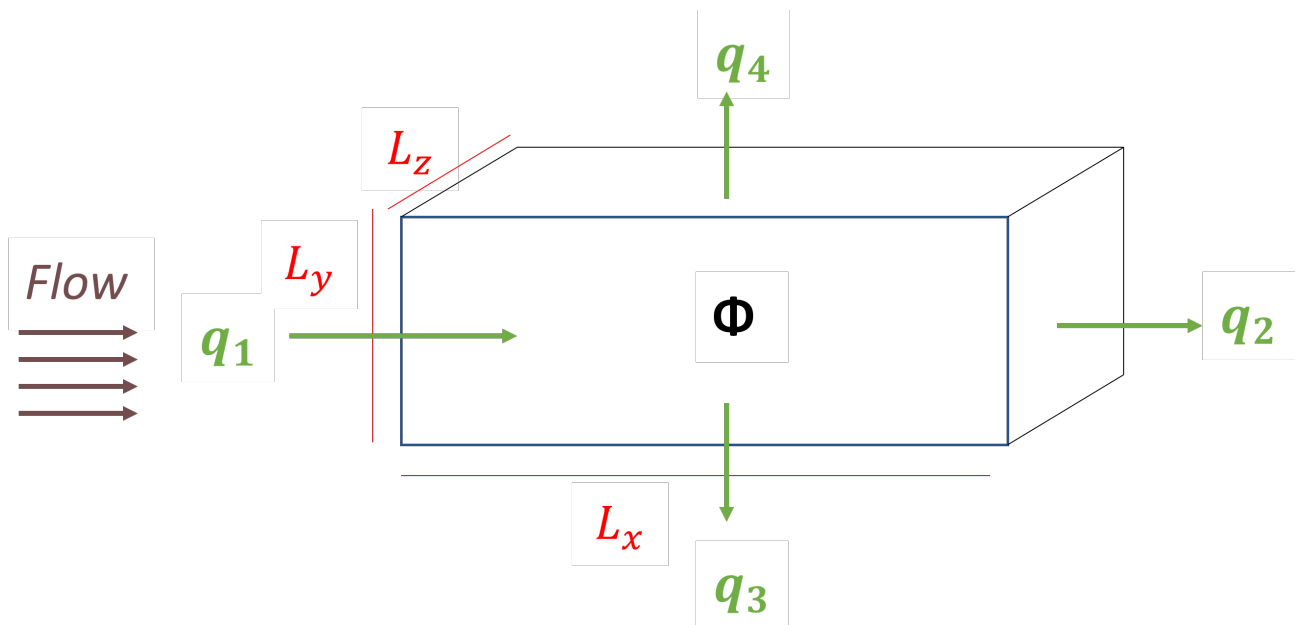


Figure 3.24: Macrobalance constructed for the calculation of the Nusselt number.

### 3.7. Does the buoyancy-aided flow promote laminarization?

Throughout the literature it is well known that during a buoyancy-assisted case, the heat transfer efficiency decreases [60]. The explanation behind this phenomenon according to Wang is the fact that there is a reduction in the shear stress, in the layer of buoyant fluid near the wall. Consequently, the production of turbulence is deteriorated and this negatively affects the diffusion of heat by turbulence. In addition, Nieuwstadt et al. [40] stated that during the buoyancy-assisted case, the time-averaged product of the fluctuation velocities which represents the Reynolds stresses, is decreased. Thus, laminarization is promoted resulting to heat transfer impairment. However, Figures 3.25 to 3.27 as well as Table 3.1 show that when the flow is buoyancy-aided, the Reynolds stresses and Nusselt number increase, indicating that the production of turbulence is increased as well as the heat transfer rate.

A possible explanation that could be given is the fact that for aided flows, buoyancy can be strong enough to create more turbulent kinetic energy instead of reducing it [6], also known as recovery. Bruch et al.[7] explained this by investigating experimentally the heat transfer characteristics of a cooled vertical turbulent flow of supercritical carbon dioxide. Particularly, he states that for low values of the mixed convection parameter  $Gr/Re^{2.7}$  (Figure 3.28), where  $Gr$  is the Grashof number, forced convection is the main mechanism of heat transfer and free convection is insignificant. This causes the parameter of the experimental Nusselt number divided by a Nusselt number calculated with pure forced convection to stay close to unity. Subsequently, as  $Gr/Re^{2.7}$  increases, buoyancy has a stronger impact on the flow and for aiding mixed convection, relaminarization occurs,  $Nu_{exp}/Nu_{FC}$  decreases and heat transfer is deteriorated. Finally, for higher values of  $Gr/Re^{2.7}$ , free convection dominates,  $Nu_{exp}/Nu_{FC}$  increases and heat transfer is improved.

To check whether the buoyancy-aided case of the current study falls within the region where free convection dominates and heat transfer is improved, the ratio  $Gr/Re^{2.7}$  is calculated via Equation (3.7)

$$\frac{Gr}{Re^{2.7}} = \frac{Ri}{Re^{0.7}} \quad (3.7)$$

The ratio of the current study is equal to 0.0019 and indeed falls in the region where free convection dominates and heat transfer is improved.

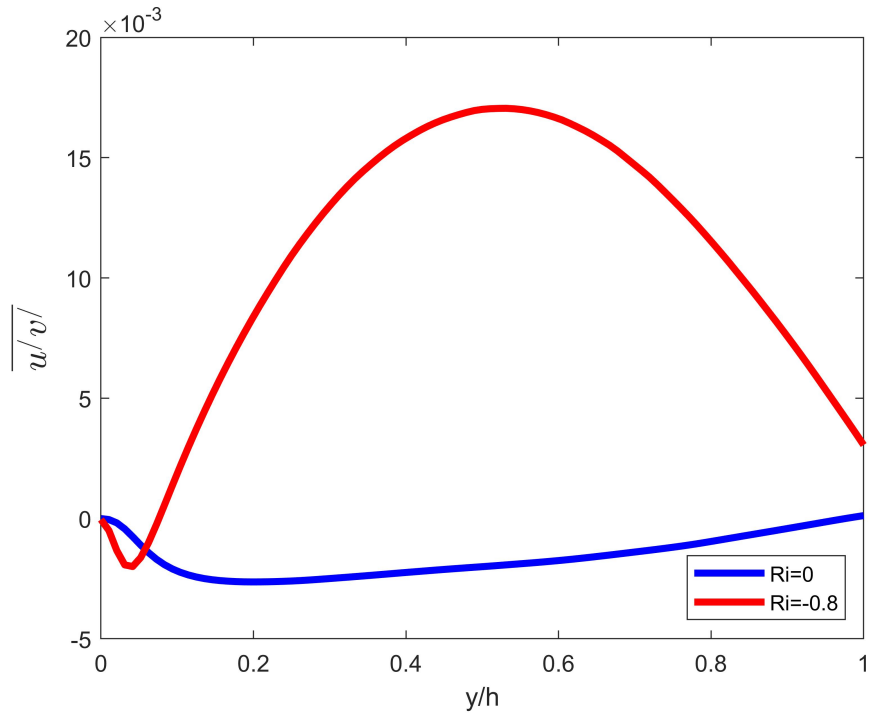


Figure 3.25: Reynolds stresses for the smooth wall case when there zero-buoyancy and when the flow is buoyancy-aided.

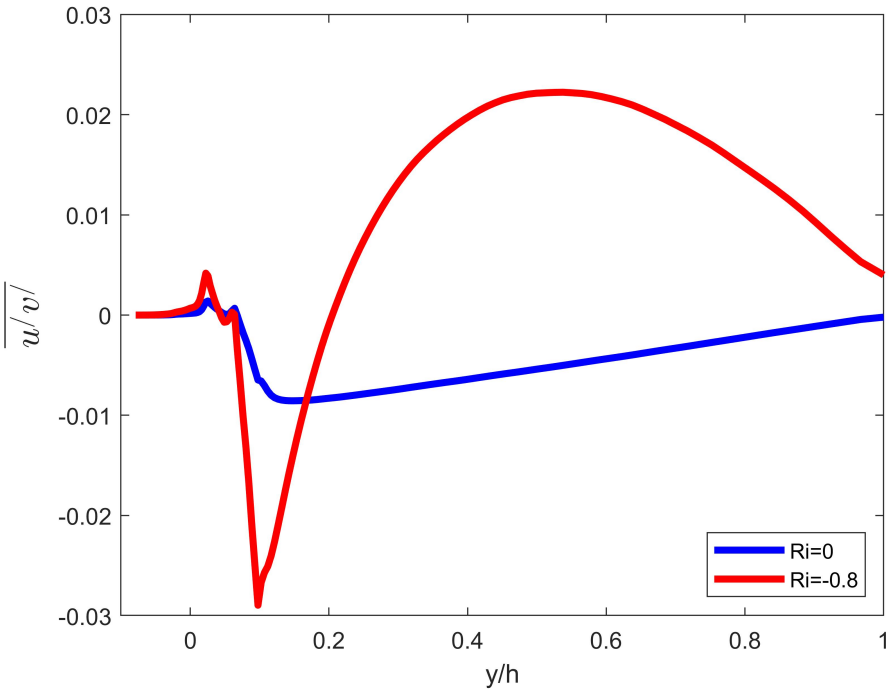


Figure 3.26: Reynolds stresses for the streamwise roughness case when there zero-buoyancy and when the flow is buoyancy-aided.

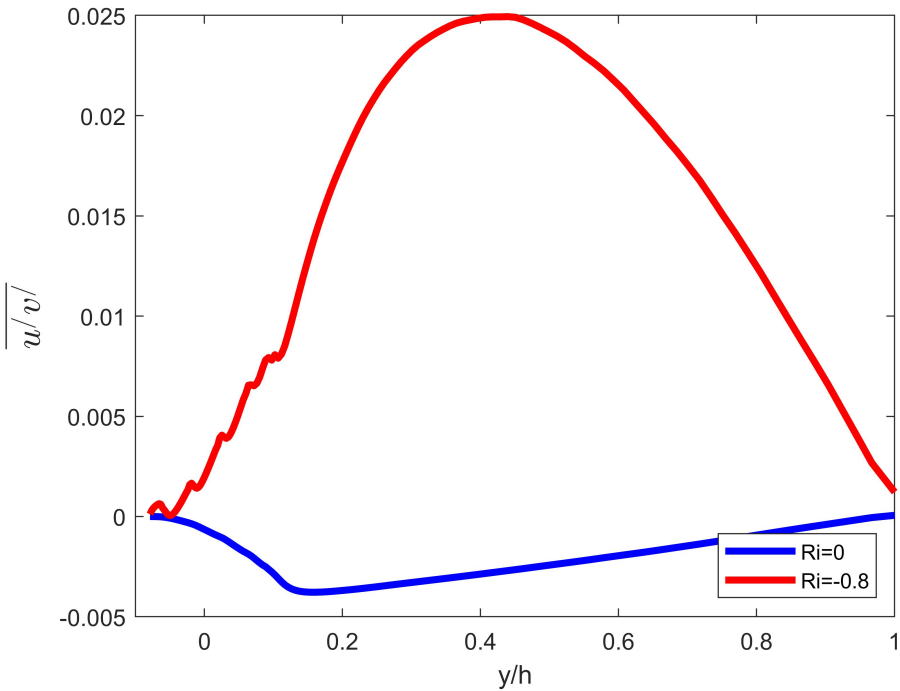


Figure 3.27: Reynolds stresses for the spanwise case when there zero-buoyancy and when the flow is buoyancy-aided.

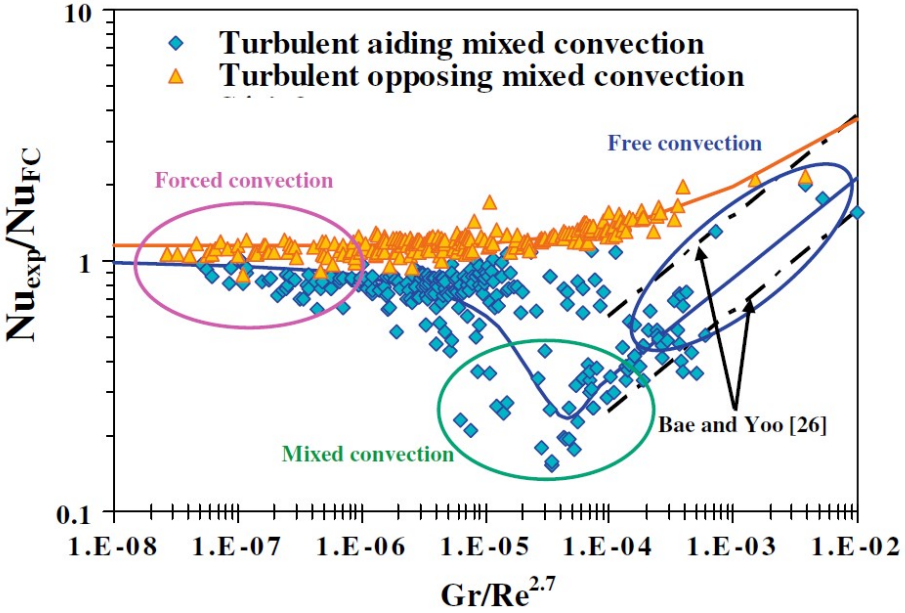


Figure 3.28: Bruch’s experimental investigation of the heat transfer characteristics of a cooled vertical turbulent flow of supercritical carbon dioxide. [6]

# 4

## Conclusions, Suggestions

### 4.1. Conclusions

The main focus of this study is to examine the impact of surface roughness and buoyancy effects on turbulent heat transfer. Initially, a 3D rectangular channel is considered with the streamwise, wall normal and spanwise dimensions being  $5.63 \times 2 \times 2.815$ . Subsequently, two different wall roughness geometries are constructed. Both of them have a sinusoidal shape, however the direction of travel is in the streamwise direction for the one and in the spanwise for the other. Moreover, the surface roughness is placed on the top and bottom isothermal walls of the geometry. Regarding the space and time discretization, central differences are used for the former one and second order Adams-Bashforth for the latter one. Finally, the immersed boundary method is utilized in order to incorporate the surface roughness.

The results display that both roughness schemes enhance heat transfer. Particularly, the Reynolds stresses show an increase in both rough wall cases, signifying that mixing is improved. In addition, the turbulent heat flux as well as the Nusselt numbers also exhibit a growth for both streamwise and spanwise orientation, implying that heat transfer is augmented.

Comparing the streamwise and spanwise orientations with each other, both Reynolds stresses and turbulent heat flux graphs are significantly higher in the streamwise roughness case. Moreover, the streamwise roughness is enhancing the Nusselt number approximately 1.8 times more than the spanwise roughness for the zero-buoyancy case and approximately 1.4 times more for the buoyancy-aided scenario.

Regarding the impact of buoyancy on the heat transfer, the results show that the buoyancy-aided case has larger Reynolds stresses, turbulent heat flux and Nusselt numbers for all of the surfaces.

## 4.2. Suggestions

Suggestions for future research are provided in this final part, in order to solve some issues that appeared and improve the final result.

It is a well-known fact that buoyancy-aided flows promote laminarization and thus heat transfer is deteriorated. However, in the current research it is presented that during the buoyancy-aided case, the Reynolds stresses, turbulent heat flux and Nusselt number increase, indicating that heat transfer is augmented. According to Bruch's experimental investigation, for strong buoyancy cases free convection dominates and heat transfer is improved. After calculating the ratio  $Gr/Re^{2.7}$ , it is observed that, having the Richardson number equal to -0.8, falls into the region where buoyancy forces are strong enough to cause heat transfer augmentation in buoyancy-aided flows. Therefore, the simulations should be repeated with a decreased Richardson number and examine for a possible reduction in the Reynolds stresses, turbulent heat flux and Nusselt number. In addition, the simulations can be repeated with positive Richardson number, to reproduce a buoyancy-opposed flow and check if heat transfer is augmented.

Another statement that exists in the literature is that, surface modifications improves the convective heat transfer, however it also increases the pressure drop. Therefore, in order to have a complete study for the particular rough surfaces, the overall enhancement ratio which is defined as the ratio of the heat transfer enhancement ratio to the friction factor ratio (Equation (1.3)) should be calculated. Subsequently, the values will be compared and at the end it will be shown whether these rough surfaces can be established in engineering applications.

# References

- [1] Olga P Arsenyeva et al. “Estimation of enhanced heat transfer area targets in process industries”. In: *Computer Aided Chemical Engineering*. Vol. 32. Elsevier, 2013, pp. 355–360.
- [2] Mark P Baldwin and Timothy M Lenton. “Solving the climate crisis: Lessons from ozone depletion and COVID-19”. In: *Global sustainability* 3 (2020).
- [3] Ergin BAYRAK, Ahmet Hakan TÜZÜN, and Ali Bahadr OLCAI. “RECENT DEVELOPMENTS IN PASSIVE HEAT TRANSFER ENHANCEMENT TECHNIQUES IN MICRO-COOLING TECHNOLOGY”. In: ().
- [4] AE Bergles. “The implications and challenges of enhanced heat transfer for the chemical process industries”. In: *Chemical Engineering Research and Design* 79.4 (2001), pp. 437–444.
- [5] Jeffrey P Bons et al. “The many faces of turbine surface roughness”. In: *Turbo Expo: Power for Land, Sea, and Air*. Vol. 78521. American Society of Mechanical Engineers. 2001, V003T01A042.
- [6] M Brocchini and DH Peregrine. “The dynamics of strong turbulence at free surfaces. Part 1. Description”. In: *Journal of Fluid Mechanics* 449 (2001), pp. 225–254.
- [7] Arnaud Bruch, André Bontemps, and Stéphane Colasson. “Experimental investigation of heat transfer of supercritical carbon dioxide flowing in a cooled vertical tube”. In: *International journal of heat and mass transfer* 52.11-12 (2009), pp. 2589–2598.
- [8] Angela Busse, Mark Lützner, and Neil D Sandham. “Direct numerical simulation of turbulent flow over a rough surface based on a surface scan”. In: *Computers & Fluids* 116 (2015), pp. 129–147.
- [9] Angela Busse, Manan Thakkar, and Neil D Sandham. “Reynolds-number dependence of the near-wall flow over irregular rough surfaces”. In: *Journal of Fluid Mechanics* 810 (2017), pp. 196–224.
- [10] Ismail Celik. *RANS/LES/DES/DNS: The future prospects of turbulence modeling*. 2005.
- [11] WM Chakroun and SF Al-Fahed. “The effect of twisted-tape width on heat transfer and pressure drop for fully developed laminar flow”. In: (1996).
- [12] Hong Cheng and Ian P Castro. “Near wall flow over urban-like roughness”. In: *Boundary-Layer Meteorology* 104.2 (2002), pp. 229–259.
- [13] P Cherukat et al. “Direct numerical simulation of a fully developed turbulent flow over a wavy wall”. In: *Theoretical and computational fluid dynamics* 11.2 (1998), pp. 109–134.

- [14] O Coceal and SE Belcher. “Mean winds through an inhomogeneous urban canopy”. In: *Boundary-Layer Meteorology* 115.1 (2005), pp. 47–68.
- [15] Ahmad Ali Rabienataj Darzi, Mousa Farhadi, and Kurosh Sedighi. “Experimental investigation of convective heat transfer and friction factor of Al<sub>2</sub>O<sub>3</sub>/water nanofluid in helically corrugated tube”. In: *Experimental thermal and fluid science* 57 (2014), pp. 188–199.
- [16] Roger Bruce Dean. “Reynolds number dependence of skin friction and other bulk flow variables in two-dimensional rectangular duct flow”. In: (1978).
- [17] Ayodeji Demuren and Holger Grotjans. “Buoyancy-driven flows Beyond the boussinesq approximation”. In: *Numerical Heat Transfer, Part B: Fundamentals* 56.1 (2009), pp. 1–22.
- [18] A Dewan et al. “Review of passive heat transfer augmentation techniques”. In: *Proceedings of the Institution of Mechanical Engineers, Part A: Journal of Power and Energy* 218.7 (2004), pp. 509–527.
- [19] Duane F Dipprey and Rolf H Sabersky. “Heat and momentum transfer in smooth and rough tubes at various Prandtl numbers”. In: *International Journal of Heat and Mass Transfer* 6.5 (1963), pp. 329–353.
- [20] Smith Eiamsa-ard, Chinarak Thianpong, and Petpices Eiamsa-ard. “Turbulent heat transfer enhancement by counter/co-swirling flow in a tube fitted with twin twisted tapes”. In: *Experimental Thermal and Fluid Science* 34.1 (2010), pp. 53–62.
- [21] Joel H Ferziger, Milovan Peri, and Robert L Street. *Computational methods for fluid dynamics*. Vol. 3. Springer, 2002.
- [22] Wanmin Gong, Peter A Taylor, and Andreas Dörnbrack. “Turbulent boundary-layer flow over fixed aerodynamically rough two-dimensional sinusoidal waves”. In: *Journal of Fluid Mechanics* 312 (1996), pp. 1–37.
- [23] RA Gowen and JW Smith. “Turbulent heat transfer from smooth and rough surfaces”. In: *International Journal of Heat and Mass Transfer* 11.11 (1968), pp. 1657–1674.
- [24] Douglas S Henn and R Ian Sykes. “Large-eddy simulation of flow over wavy surfaces”. In: *Journal of Fluid Mechanics* 383 (1999), pp. 75–112.
- [25] MH Hosni et al. “Roughness element shape effects on heat transfer and skin friction in rough-wall turbulent boundary layers”. In: *International Journal of Heat and Mass Transfer* 36.1 (1993), pp. 147–153.
- [26] JD Jackson. “Fluid flow and convective heat transfer to fluids at supercritical pressure”. In: *Nuclear Engineering and Design* 264 (2013), pp. 24–40.
- [27] JD Jackson, MA Cotton, and BP Axcell. “Studies of mixed convection in vertical tubes”. In: *International journal of heat and fluid flow* 10.1 (1989), pp. 2–15.
- [28] Wen-Tao Ji et al. “Summary and evaluation on single-phase heat transfer enhancement techniques of liquid laminar and turbulent pipe flow”. In: *International Journal of Heat and Mass Transfer* 88 (2015), pp. 735–754.

- [29] Binfan Jiang et al. “Efficient waste heat recovery system for high-temperature solid particles based on heat transfer enhancement”. In: *Applied Thermal Engineering* 155 (2019), pp. 166–174.
- [30] Yan Jin and Heinz Herwig. “Turbulent flow in rough wall channels: Validation of RANS models”. In: *Computers & Fluids* 122 (2015), pp. 34–46.
- [31] Satish G Kandlikar et al. “Characterization of surface roughness effects on pressure drop in single-phase flow in minichannels”. In: *Physics of Fluids* 17.10 (2005), p. 100606.
- [32] Nobuhide Kasagi and Mitsugu Nishimura. “Direct numerical simulation of combined forced and natural turbulent convection in a vertical plane channel”. In: *International Journal of Heat and Fluid Flow* 18.1 (1997), pp. 88–99.
- [33] Pawan Singh Kathait and Anil Kumar Patil. “Thermo-hydraulic performance of a heat exchanger tube with discrete corrugations”. In: *Applied Thermal Engineering* 66.1-2 (2014), pp. 162–170.
- [34] John Kim, Parviz Moin, and Robert Moser. “Turbulence statistics in fully developed channel flow at low Reynolds number”. In: *Journal of fluid mechanics* 177 (1987), pp. 133–166.
- [35] Xiao-wei Li, Ji-an Meng, and Zeng-yuan Guo. “Turbulent flow and heat transfer in discrete double inclined ribs tube”. In: *International Journal of Heat and Mass Transfer* 52.3-4 (2009), pp. 962–970.
- [36] Q Liao and MD Xin. “Augmentation of convective heat transfer inside tubes with three-dimensional internal extended surfaces and twisted-tape inserts”. In: *Chemical Engineering Journal* 78.2-3 (2000), pp. 95–105.
- [37] Leon Liebenberg and Josua P Meyer. “In-tube passive heat transfer enhancement in the process industry”. In: *Applied Thermal Engineering* 27.16 (2007), pp. 2713–2726.
- [38] Carsten MaaSS and Ulrich Schumann. “Direct numerical simulation of separated turbulent flow over a wavy boundary”. In: *Flow Simulation with high-performance computers II*. Springer, 1996, pp. 227–241.
- [39] Bashir Muhammad. “Energy consumption, CO<sub>2</sub> emissions and economic growth in developed, emerging and Middle East and North Africa countries”. In: *Energy* 179 (2019), pp. 232–245.
- [40] Frans TM Nieuwstadt, Jerry Westerweel, and Bendiks J Boersma. *Turbulence: introduction to theory and applications of turbulent flows*. Springer, 2016.
- [41] Johann Nikuradse et al. “Laws of flow in rough pipes”. In: (1950).
- [42] Tomás Norton and Da-Wen Sun. “Computational fluid dynamics (CFD)—an effective and efficient design and analysis tool for the food industry: a review”. In: *Trends in Food Science & Technology* 17.11 (2006), pp. 600–620.
- [43] P Orlandi, D Sassun, and S Leonardi. “DNS of conjugate heat transfer in presence of rough surfaces”. In: *International Journal of Heat and Mass Transfer* 100 (2016), pp. 250–266.

- [44] P R Owen and WR Thomson. “Heat transfer across rough surfaces”. In: *Journal of Fluid Mechanics* 15.3 (1963), pp. 321–334.
- [45] JWR Peeters and ND Sandham. “Turbulent heat transfer in channels with irregular roughness”. In: *International journal of heat and mass transfer* 138 (2019), pp. 454–467.
- [46] IA Popov, Yu F Gortyshov, and VV Olimpiev. “Industrial applications of heat transfer enhancement: The modern state of the problem (a Review)”. In: *Thermal Engineering* 59.1 (2012), pp. 1–12.
- [47] RC Prasad and Jihua Shen. “Performance evaluation of convective heat transfer enhancement devices using exergy analysis”. In: *International Journal of Heat and Mass Transfer* 36.17 (1993), pp. 4193–4197.
- [48] Pongjet Promvong et al. “Heat transfer augmentation in a helical-ribbed tube with double twisted tape inserts”. In: *International Communications in Heat and Mass Transfer* 39.7 (2012), pp. 953–959.
- [49] Gabriela Aparecida dos Reis et al. “A compact finite differences exact projection method for the Navier–Stokes equations on a staggered grid with fourth-order spatial precision”. In: *Computers & Fluids* 118 (2015), pp. 19–31.
- [50] W Rodi. “Comparison of LES and RANS calculations of the flow around bluff bodies”. In: *Journal of wind engineering and industrial aerodynamics* 69 (1997), pp. 55–75.
- [51] WF Scaggs, Robert P Taylor, and Hugh W Coleman. “Measurement and prediction of rough wall effects on friction factor Uniform roughness results”. In: (1988).
- [52] Muhammad Shahbaz and Hooi Hooi Lean. “Does financial development increase energy consumption? The role of industrialization and urbanization in Tunisia”. In: *Energy policy* 40 (2012), pp. 473–479.
- [53] Thorsten Stoesser. “Physically realistic roughness closure scheme to simulate turbulent channel flow over rough beds within the framework of LES”. In: *Journal of Hydraulic Engineering* 136.10 (2010), pp. 812–819.
- [54] Kennet J Stout, EJ Davis, and P Sullivan. *Atlas of machined surfaces*. Springer Science & Business Media, 2012.
- [55] Dawid Taler and Jan Taler. “Simple heat transfer correlations for turbulent tube flow”. In: *E3S Web of conferences*. Vol. 13. EDP Sciences. 2017, p. 02008.
- [56] Tetsuro Tamura, Shuyang Cao, and Azuma Okuno. “LES study of turbulent boundary layer over a smooth and a rough 2D hill model”. In: *Flow, turbulence and combustion* 79.4 (2007), pp. 405–432.
- [57] Manan Thakkar, Angela Busse, and Neil Sandham. “Surface correlations of hydrodynamic drag for transitionally rough engineering surfaces”. In: *Journal of Turbulence* 18.2 (2017), pp. 138–169.
- [58] RL Townsin. “The ship hull fouling penalty”. In: *Biofouling* 19.S1 (2003), pp. 9–15.
- [59] Martin Wahl. “Marine epibiosis. I. Fouling and antifouling: some basic aspects”. In: *Marine ecology progress series* 58 (1989), pp. 175–189.

- 
- [60] Jinlei Wang, Jiankang Li, and John Derek Jackson. “A study of the influence of buoyancy on turbulent flow in a vertical plane passage”. In: *International Journal of Heat and Fluid Flow* 25.3 (2004), pp. 420–430.
- [61] ZJ Wang et al. “Direct Simulation of Surface Roughness Effects with a RANS and DES Approach on Viscous Adaptive Cartesian Grids”. In: *34th AIAA Fluid Dynamics Conference and Exhibit*. 2004, p. 2420.
- [62] Ralph L Webb. “Single-phase heat transfer, friction, and fouling characteristics of three-dimensional cone roughness in tube flow”. In: *International Journal of Heat and Mass Transfer* 52.11-12 (2009), pp. 2624–2631.
- [63] Zhengtong Xie and Ian P Castro. “LES and RANS for turbulent flow over arrays of wall-mounted obstacles”. In: *Flow, Turbulence and Combustion* 76.3 (2006), pp. 291–312.
- [64] Jianming Yang and Elias Balaras. “An embedded-boundary formulation for large-eddy simulation of turbulent flows interacting with moving boundaries”. In: *Journal of Computational Physics* 215.1 (2006), pp. 12–40.
- [65] Xiaodong Zhang and Sandip Dutta. “Heat transfer analysis of buoyancy-assisted mixed convection with asymmetric heating conditions”. In: *International journal of heat and mass transfer* 41.21 (1998), pp. 3255–3264.
- [66] Bahman Zohuri. “Compact heat exchangers design for the process industry”. In: *Compact Heat Exchangers*. Springer, 2017, pp. 57–185.